Microwavave Tomography for Breast Cancer Detection

Master's thesis in Master's of Biomedical Engineering

Maryam Naseri

Microwave Tomography for Breast Cancer Detection

Maryam Naseri

Microwave Tomography for Breast Cancer Detection

Maryam Naseri

Cover: the cover shows the antenna array and reconstruction results of dielectric properties of a cup of sunflower oil.

In memory of my father
To my mother and Mohammad

Abstract

Breast cancer is the second-leading cause of female death around the world. Recent researches in United States and several European countries state that significant number of women face this problem. However this kind of cancer can be cured with effective treatments if it is diagnosed in early stage. Several breast screening methods such as X-ray based mammography, ultrasound and Magnetic Resonance Imaging (MRI) exist for breast tumour examination. It should be taken into consideration that screening methods should have high specificity and sensitivity to malignant tumours. Furthermore, these methods have to satisfy some conditions such as comfort of the patient during imaging, high resolution images for more accurate interpretation, cost and ability to detect the malignant tumours in early stage. The mentioned imaging modalities do not meet all of these conditions simultaneously. A new approach dealing with breast cancer is microwave imaging. Microwave imaging is an iterative nonlinear reconstruction algorithm, which uses electromagnetic radiation with frequencies around 1 GHz. As this method utilizes non-ionizing radiation, it is an efficient and safe technique for breast cancer detection. Principle of this technique relies on the significant contrast between the dielectric properties of tumours and healthy tissues at microwave frequencies. In Tomography technique, different slices of an object are created by measuring the transmitted and reflected penetrating waves to the object. In microwave tomography the breast is monitored with magnetic field and properties of breast are reconstructed by evaluating the scattered electromagnetic signals. In this thesis work, 24 monopole antennas are placed around the object and scattered field is measured when transmitted waves interact with an object in microwave tomography setup. In the following, different simulations are made by using FDTD method to model the antennas and reconstruction domain. The reconstruction algorithm uses inverse problem algorithm to define a feature of dielectric properties of the target object.

Several measurements are performed with current microwave setup for imaging the modelled breast phantoms. Appropriate frequency components and reconstruction setting have been evaluated for different large and small objects in several medium.

The permittivity of one large object and two small objects were reconstructed successfully. Several breast models including different sizes of tumours were simulated with the existent algorithm. Reconstruction of dielectric properties of simulated data show good agreement with original models.

Key words:

3D microwave tomography, FDTD method, antenna modeling, mammography, breast cancer

Acknowledgement

Contents

1 Introduction

This chapter aims at giving an introduction to basics of microwave imaging. It is also a review of Microwave Tomography and explanation of the principles of Microwave Tomography application for breast cancer detection. In the following the breast anatomy and different types of breast cancer will be described.

1.1 Microwave tomography

The concept of microwave imaging and electromagnetic waves have attracted attentions from many research areas in recent decades. Microwave imaging is using to study the dielectric properties of an object in the microwave frequency range which is in the range around 1 GHz [1]. In Biomedical applications, microwave imaging techniques are classified into two main categories, namely: active and passive microwave imaging. The principles of active imaging technique is based on illuminating the desired object through the measurement system. On the other hand, in the passive imaging system the imaged object radiates energy as low level. The measured temperature of a living human tissue is an illustration of low-level EM fields which are radiated from imaged tissue. Microwave radiometry is an example of this technique [2]. There are two main methods in active microwave imaging; microwave tomography (MWT) [3], [4] and radar microwave imaging [5]. The main focus of this master thesis is on active microwave imaging systems, MT.

In microwave imaging electromagnetic waves propagate in frequency ranges of 1 GHz.The mentioned waves can go through the human body tissues and scattered signals can represent the structure and map electrical properties of tissues. There are several applications using microwaves for defining unknown objects for different aims such as detecting weapons, non-destructive testing of materials, and navigation system such as GPS. Microwaves applications have been used to determine the dielectric properties of living tissues such as skin, fat, muscle and etc.

1.2 Related works

In 1970s, for the first time, Larsen and Jacobi developed an antenna system, using two antennas, one for transmitting and the other for receiving, to measure the transmission coefficients and utilize them for imaging the canine kidney. The setup system included the two antennas, with the imaged target immersed in a tank filled with water as matching liquid to generate 2-D images. With this setup they were able to experimentally make images of a canine kidney, explained in [6].

In another study performed by Semenov et al. the measurement system consisted of 64 waveguide antennas, 32 as transmitter and 32 as receiver in a circular array. In this study the frequency of 2.45 GHz was used to reconstruct canine hearts, and beating canine hearts images [7]. The aim of this experiment was investigating the possible ways to use 2D diffraction models for constructing 2D images. To do this, a 3D target object was imaged in X-ray tomography systems. The result of the study proved that it is not possible to create 3D quantitative images by using the principle of 'slice' in X-ray tomography modality. So, a 3D system is required for this purpose.

The planar microwave imaging system is another researches topics in microwave imaging, explained in [8]. In this case, two horn antennas were utilized for measurement system, one of the antennas as transmitter and the other as receiver.

Meany et al. performed a research study to reconstruct 2D images of dielectric properties in human tissues. In his research the measurement system utilized 4 waveguide antennas as transmitters and 4 monopole antennas as receivers in a circular pattern. The functional frequency of measurement system was between $300 - 1100$ MHz [9].

In 2000s, Meany et al. developed a clinical prototype for 2D microwave imaging system [10]. The configuration of this system comprised 16 monopole antennas, which all operate as transmitters and receivers in a circular pattern. The reason for applying monopole antennas in this study, was that the monopole antennas can be modelled and operated as a line source and have acceptable radiation in lossy mediums, such as breast. The principle concept of this work is based on their earlier research [11], [12]. The measurement system is mounted on a transportable bed, which includes a hollow part for placing the circular measurement system. The patient's breast is suspended in the circular shaped antenna system to be imaged. The experiment was performed on five patients and 2D images with satisfying accuracy were acquired from real breast tissues.

In recent years, several studies have been made in 3D image reconstruction. The aim of extending to 3D imaging system was achieving accurate and high resolution images of dielectric properties distribution. The price that has to be paid when moving from 2D to 3D modelling system is the heavy computational load that requires high performance computers to solve the calculations. Several recent studies in 3D are described in more details in the literature [8], [13-16]. Various iterative nonlinear methods are applied to reconstruct dielectric parameters of the target object.

The reconstruction algorithm that is used in this master thesis will be discussed more in details in part 4, image reconstruction.

MWT known as quantitative imaging methods (also called inverse scattering methods) can be used as diagnostic tool for breast cancer imaging, lung cancer imaging and brain imaging. In MWT method an unknown object is illuminated by one or several transmitter antennas, and the object is detected by measuring the scattered signals from the object.

MWT system consists of two main parts which are known as software and hardware and will be discussed in details in sections 3, 4 and 6. Briefly, in hardware parts, the system consists of 24 monopole antennas which are used both as transmitters and receivers to propagate electromagnetic waves through the target and collect the measured data from the object. Besides, in the software part, the measured data will be processed by a different reconstruction algorithms, which is developed by A.fhager [17], to give a clear image of detected target object.

1.3 Microwave Tomography and breast cancer detection

Recent studies shows that, after lung cancer breast cancer is the most widespread cancer type among women in the United States [18]. The condition is also same in Sweden. According to national official statistics of Sweden, breast cancer is the most frequent cancer among women indicating 30.3% of all cancer cases in 2011[19]. However, if the cancer is detected in an early stage, it can be treated, and the earlier that is detected the greater the chances of the success. Efficient screening methods play an important role in reducing the mortality and detecting tumours in early stages. Screening methods should meet some conditions in the following; (i) high resolution between malignant

and healthy tissue in order to obtain more accurate diagnosis by the physicians, (ii) comfort of the patient during monitoring, (iii) affordable costs (iv) low radiation dose(v) high sensitivity and specificity.

Nowadays, X-ray based mammography is the gold standard for breast cancer detection. However this screening method is not extremely efficient due to some shortcomings described in the following.

First of all, mammography system applies high ionizing radiation that can cause serious health problems. Furthermore, it compresses breast between two plates which can be painful and dis-comfortable so it is not fascinating for most of women. Although mammography is the most common screening method, it is not able to detect fast – growing cancerous regions in pre-invasive phase [20]. In addition, mammography imaging system includes high false – negative rates: this amount is 20% in the women under age of 60 and more than 40% in women under age of 50, due to dense breasts which include large amount of fibroglandular tissues [21], [22]. This technique also contains high false – positive rate which is approximately 50% and leads to application of open surgical biopsy for more accurate diagnosis. Open surgical biopsy is an invasive procedure which is carried out in operation rooms and needs general anaesthesia. In breast biopsy test, the fluid or a part of suspicious tissue is sampled to be analysed under microscope. It is a reliable way to diagnosis the cancerous area but also it is expensive and painful. Needle biopsy is another type of biopsy which is less invasive and cheaper and doesn't need general anaesthesia so the recovery time is shorter in this method. Though, it has a lesser amount of accuracy in comparison with open surgical biopsy and it is due to limited sampling data from suspicious region. Also, it is found that the false – negative rate is between 1% and 7% in the biopsy method used together with mammography modality [23].

Currently several tomographic imaging modalities such as Computed Tomography (CT), Positron Emission Tomography (PET) and Magnetic resonance Imaging (MRI) are used for monitoring different tissues within the body. Each of these methods has their own advantages and disadvantages. For instance, although CT is an effective imaging technique, it is not very functional in soft tissues and suffers from low specificity which can make non-functional results of malignancies tissue. Also it contains high radiation dose, which may cause serious health problems in the patients. On the other hand, MRI technique which applies radio waves can be used for medical imaging as it provides very detailed diagnostic images even in soft tissues. For breast imaging procedure with MRI usually a contrast material, gadolinium, is injected through the vein in the arm before and during the imaging process to improve the contrast (or specificity) images of breast tissue. One should also bear in mind that the high sensitivity of MRI system is not an advantage all the time because in some situations the tissue detected as abnormal are not cancerous. This occasion induce unnecessary treatments for patients. Moreover, patients with metal implants within their body are not able to be imaged with this high cost effective imaging method.

The discussed techniques in the above don't meet all the conditions for desired technique for breast cancer detection.

Microwave Tomography (MWT) could potentially become a complementary technique for diagnosing malignant tissues. Microwave images introduce the map of dielectric properties of an object. Permittivity and conductivity are two parameters which describe propagation of microwave signals in the materials. In the microwave frequency range, different biological tissues demonstrate specific behaviours based on their dielectric properties. It is so known that dielectric properties of high water content tissues (such as blood and cancerous tissues) and low water content tissues (such as fat

and skin) differ significantly meaning that there is a high contrast in permittivity and conductivity of malignant and healthy breast tissues. It is known that low water content tissues have lower permittivity values in comparison to high water content tissues [24], [25].

1.3.1 Challenges in MWT

The principle of microwave tomography is based on the contrast between dielectric properties of malignant and normal tissues. It should be taken in consideration that the tissues within the body are inhomogeneous and their properties change during the life time. The breast is a very loosy tissue and due to this reason permeability of microwave frequencies is restricted. The other important challenge in this study is determining the measurements of in vivo tissue properties, this process is challenging due to the limitation to access to in vivo tissues but the dielectric parameters should be assumed carefully to give the most accurate measurements regarding to get as close as simulated objects to real tissue[26]. Likewise, the calibration of the system and E-field measurements should be carried out precisely to approach as less amount of errors as possible. Furthermore, the speed of reconstruction is low due to the utilization of inverse imaging algorithms and heavy computational equations to be solved in order to detect the unknown object.

Developments in the image reconstruction algorithms and measurements setup can make MWT systems a powerful alternative for breast cancer detection.

1.3.2 Purpose

The aim of the project is improving the current microwave diagnostic procedure by using reconstruction imaging algorithms to reach better contrast and detection in comparison with available methods. The main goal in this master thesis is finding appropriate parameters for frequency components corresponding to the dielectric properties of different materials and obtaining the desired setting for the reconstruction of different materials in order to make breast mimicking prototype. To this end several breast models including different sizes of tumours were simulated with the existent algorithm. In the experimental part, different measurement is done with existence prototype and results were evaluated with the available 3D image reconstruction algorithm.

1.4   Breast anatomy

A female breast is composed of glandular tissue, fat, ducts, lymph vessels, ligaments, fibrous connective tissue and lymph nodes. The composition of breast tissues vary among women. The proportion of glandular, adipose and connective tissues differ in each woman. Figure 1.4-1demonstrates the details of a female's healthy breast.
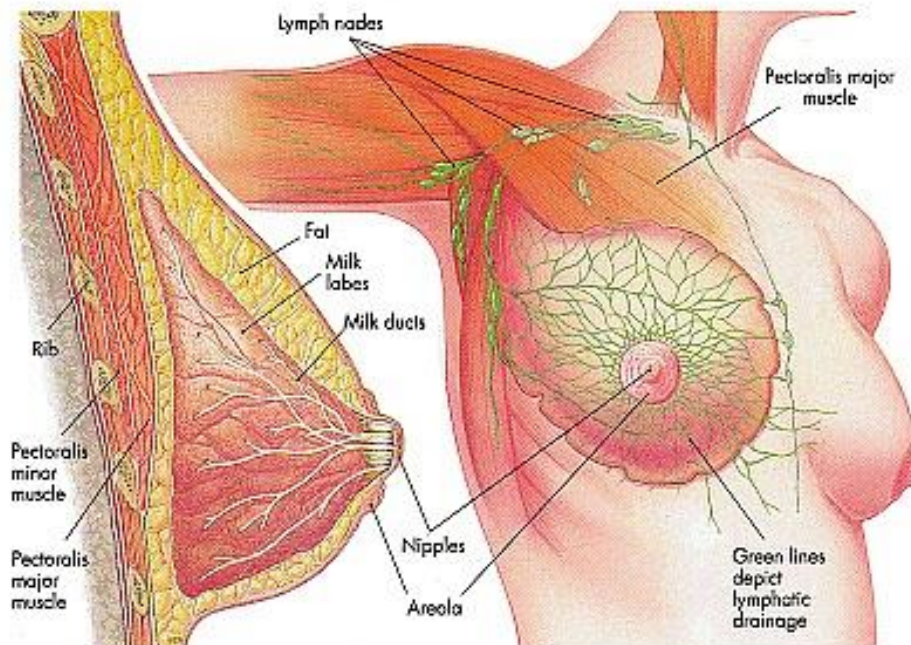

Figure 1.4-1 Anatomy of a female's breast (taken from http://nursingcrib.com/anatomy-and-physiology[27])

As seen in Figure 1.4-1 fatty tissues, which is also called adipose tissues expands from collarbone to the downside of the ribs cage and fills the spaces around the ducts and lobules. Each breast is then made of other parts such as lobes, lobules and milk ducts. The lobes and lobules connect through the milk ducts. Lobes consist of smaller lobules and contain groups of tiny milk producing glands. The number of lobes in a normal and healthy breast tissue are between 12 and 20. The lobules function is producing milk in nursing women. After delivery, the produced milk passes through the ducts into the nipple to feed the baby. In addition, fibrous connective tissues have the function of supporting the breast and firm it. The lymph nodes play an important role to diagnose cancer. The lymph is known as yellow fluid that circulates in the lymphatic system and finally is drained to the vein. The function of this system is carrying the bacteria and wastes out of the human body. Briefly, lymph nodes act as filters in the body. In the case of cancer, the cancerous cells break and move to the closest lymph node via flowing tissue fluid, so the doctors can examine the lymph glands in the early stages to determine whether the patient is cancerous or not. Breast cancer commonly develops in the lobules, glands and ducts of the breast.

1.4.1   Breast cancer

Breast cancer is the most common cancer among women today, stated in [18], [19]. The breast cancer is an abnormality in the breast tissues, it mostly grows in fatty tissues and lobules and in the worst cases it spreads to other organs and cause incurable metastasis. The breast connects to small masses of tissue called lymph nodes through the lymph vessels. The lymph nodes are responsible for collecting the bacteria, cancer cells and

other unhealthy materials. There are groups of lymph nodes under the arms and above the collarbones as well as in other parts of the body.

The extent of disease is describing by its stage. The cancer stage is based on several factors, containing: (i) the size of the tumour if any lymph node is involved, (ii) if the cancer is invasive or non-invasive and (iii) if the cancer has spread on the areas beyond the breast.

According to this explanation, the stage of breast cancer is divided into three phases.

Stage 0 is considered as non-invasive. In this stage there is no evidence of cancer cells which have spread to neighbouring breast tissue beyond the duct or lobule. This case can be cured by radiation or surgery or a combination of both procedures. Stage1 is considered as early stage of invasive breast cancer; the measured diameter of the tumour is not more than 20mm and there is no evidence that the cancer cells have spread beyond the breast. Stage 2 is divided into two sub groups: 2a and 2b. It is still a curable stage and patient can be cured by specific treatments. Stage 2a is an invasive breast cancer either with a maximum diameter of 20mm and spread to the lymph nodes under the arm, or the size of tumour is between 20-50mm and has not extended to any lymph nodes.

The situation is a bit different in stage 2b. In this case the diameter of tumour is between 20-50mm and the cancerous part has spread under arm lymph nodes, or in the other occasion the tumour size is larger than 50mm in diameter and has not spread to any lymph nodes under arm. Further, stage 3 is referred to locally advance cancerous cells. It is also divided into 3 sub categories, 3a, 3b and 3c. In the case of 3a stage two classes of breast cancer can be described. In first occasion, the tumour is not larger than 50 mm in the diameter but it has spread under the arm lymph nodes and are growing into each other forming mass of cancerous cell and it is also can be spread along the lymph nodes near to the breast bone, in the second class of this sort of cancerous cells the lymph nodes are not involved with abnormalities. In stage3b, the tumour can be of any size and unlike the other types of tumours it can expand to the skin and chest wall and may cause swallowing in the breast skin. In 3c, the tumour also can be any size but it expands to lymph nodes which spread below or above the clavicle, the chest wall and skin of breast. The last stage, stage4, is known as distinct metastasis cancer, which means that cancer cells have diffused to other organs of the body such as lungs, bones and brain [18]. Based on our research, unfortunately there is no treatment for this stage of breast cancer up to today.

2 Dielectric Properties

In this section, the dielectric properties of the biological tissues will be discussed. Afterwards, the structure of dispersive properties and their manner in the different substances will be described.

2.1 Introduction to dielectric properties

At microwave frequencies electromagnetic radiation penetrates to the biological tissues. The impact of this interaction is visible at cellular and molecular levels and demonstrates the energy depositions in a living tissue. Permittivity and conductivity are two main dielectric properties which play an important role in characterizing different materials.

The permittivity determines how the material is affected and polarized by the applied electric field. In another word, applying an external electric field to a material leads to create current in that material. The conductivity defines that how much a material can conduct the current and also provides electrical losses in that material. The basics of dielectrics properties are explained in the section 2.2.

2.2 Complex dielectric properties

The dielectric properties of a tissue can be determined by measuring the complex relative permittivity, ϵ, of the material, defined as,

$$\epsilon = \epsilon' - j\,\epsilon'' \qquad (2.2.1)$$

Where ϵ', represents the relative permittivity, $j = \sqrt{-1}$ and ϵ'' is dielectric loss coefficient and can be written as,

$$\epsilon'' = \frac{\sigma}{\epsilon_0 \omega} \qquad (2.2.2)$$

As it is indicated in equation (2.2.2), the loss factor is a function of conductivity and frequency. Furthermore, ϵ_0 and ω represent the permittivity of free space and angular frequency of the field respectively. The conductivity expressed in Siemens per minute (S/m), ϵ_0 is expressed in farads per meter (F/m) and ω in radians per second (rad/sec). Figure 2.2-1(a) and (b) shows the frequency dependence of dielectric properties of different tissues modelled by Gabriel et al., [28]
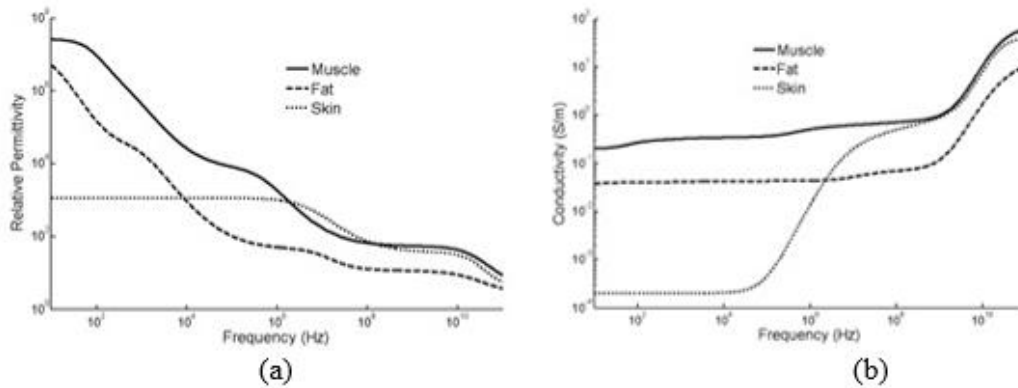
Figure 2.2-1 Curves for complex permittivity of different human tissues at 37°C, modelled by Cole-Cole equation, investigated by Mohammad Mahfuz [29].(a)Relative permittivity, (b) conductivity

As seen in the Figure 2.2-1, with increasing the frequency the dielectric constant decreasing, while the situation is opposite for the conductivity values.

2.3 Dispersive response

The dielectric parameters are strongly dependent on frequency. Frequency dispersion indicates the frequency dependency of a biological tissue. The frequency dispersion of dielectric properties is divided into three main regions, $\alpha\,(alpha), \beta\,(beta)$ and $\gamma\,(gamma)$.

In the following, the three regions of dispersion will be explained briefly.

Alpha dispersion: this frequency spectrum is due to the ionic diffusion which illustrates the interaction of the intracellular organelles and outer cell membranes. The functional area of alpha dispersion is in low frequencies which are between a few Hz and KHz.

Beta dispersion: beta dispersion is placed in the radio frequency (RF) limited area, which is between 10 kHz and 10 MHz. By increasing the electromagnetic frequency the cellular membranes become as short-circuited systems. This phenomenon causes a decrease in the effects of bound water insulating, and an increment in conduction through cell membrane. Conductivity rises as a result of this principle in beta dispersion.

Gamma dispersion: the dielectric parameters in the body tissues are studied according to their molecules of water. Gamma dispersion is the result of the dipolar relaxation of free water and appears in the centre frequency of about 25GHz at body temperature, 37°C. This is the studied frequency region in microwave research. Behaviour of water content tissues are observed in this frequency span. The frequency band for gamma dispersion is higher than 100MHz.

Figure 2.3-1 is a comparison of frequency dispersion values of different healthy and malignant tissues literature by Andreas Fhager [17].
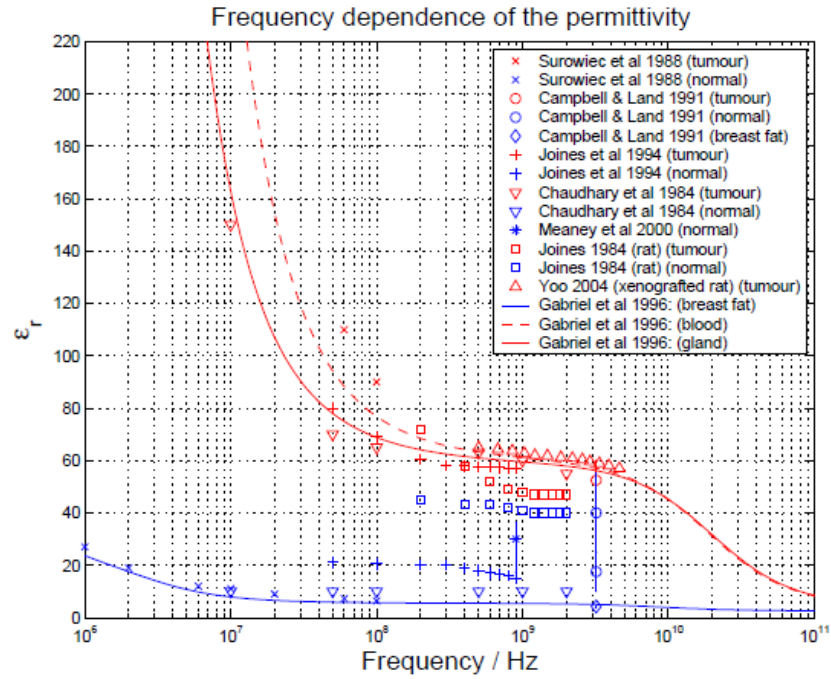
(a)
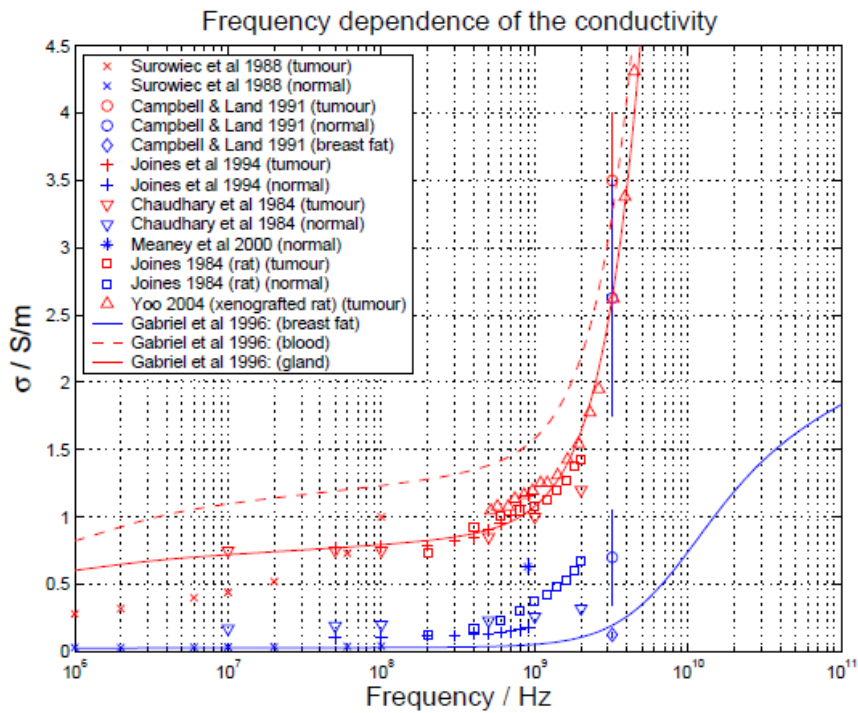
(b)

Figure 2.3-1 Literature values for conductivity and permittivity by A. Fhager [17]. (a) Frequency dependency of the permittivity, (b) Frequency dependency of conductivity. The red signs illustrate malignant tissues and blue ones are representing normal, healthy tissues.

2.4 Dielectric model of relaxation response

Molecules and ions contained in a material will be charged by applying an electrical field. However, this procedure is not instant and its simulation requires a model that explains how the dielectric parameters vary in different times.

Debye developed a model which explains the dispersive response of the dielectric parameters on a molecular level [30]. The Debye equation is shown in the following,

$$\epsilon^*(\omega) = \epsilon_{inf} + \frac{\epsilon_{static} - \epsilon_{inf}}{1 + i\omega\tau} \qquad (2.4.1)$$

Where ϵ^* determines the complex dielectric constant, ϵ_{static} and ϵ_{inf} are the static and infinite frequency dielectric constants, ω represents the angular frequency and τ is a time constant.

Static conductivity is added to equation (2.4.1) for including the current at infinite times and ion drifts in the constant field. The equation becomes,

$$\epsilon^*(\omega) = \epsilon_{inf} + \frac{\epsilon_{static} - \epsilon_{inf}}{1 + i\omega\tau} - \frac{\sigma_{static}}{\omega\tau} \qquad (2.4.2)$$

It was later discovered that human tissues have more than one relaxation frequency and because of this fact Debye's equation is not appropriate to describe this phenomenon. Cole Cole has derived an empirical function, which is able to model the dielectric properties of different tissues [31], [32],

$$\epsilon^*(\omega) = \epsilon_{inf} + \sum_n \frac{\Delta\epsilon_n}{1 + (i\omega\tau_n)^{(1-a_n)}} + \frac{\sigma_{static}}{i\omega\epsilon_0} \qquad (2.4.3)$$

The values for dielectric parameters are provided by performing measurements to obtain the accurate data to insert in equation (2.4.3)

3 Materials and Methods

In this chapter the electromagnetic model, computation of the propagating electromagnetic fields in a material and simulation procedure will described in detail.

3.1 The FDTD Method

The Finite-Difference Time-Domain is a numerical technique for solving Maxwell's equations. The reputation of this technique is because of simplicity and efficiency even in complex and realistic problems. In this section FDTD method will be described in detail.

3.1.1 Maxwell's Equations

The whole of electromagnetic theory is based on Maxwell's equations. They are a set of 4 equations describing the propagation and interaction of electric and magnetic fields [33],

$$\nabla . D = \rho, \tag{3.1.1}$$

$$\nabla . B = 0, \tag{3.1.2}$$

$$\nabla \times E = -\frac{\partial B}{\partial t}, \tag{3.1.3}$$

$$\nabla \times H = \frac{\partial D}{\partial t} + J_e . \tag{3.1.4}$$

Where, D represents the electric displacement, E is the electric field strength, B is the magnetic flux density, H is the magnetic field strength and J_e indicate the electric losses in a medium.
The dielectric parameters of different substances can represent the properties of the substances. The following equations are used for this purpose,

$$D = \epsilon E , \tag{3.1.5}$$

$$B = \mu H, \tag{3.1.6}$$

$$J_e = \sigma E, \tag{3.1.7}$$

The permittivity, ϵ expresses the amount of resistance, while applying an external electrical field in an insulator. The presence of an external electrical field induces the molecules of dielectrics to polarize in a particular way, which cause minimization in the electrical field inside the material. In a similar way, the permeability, μ, is equivalent of permittivity values for the magnetic field instead of electrical field. The permeability illustrates the measure of magnetization of a material while exposed to a magnetic field. Furthermore, the conductivity, σ, indicates the ability of the material to conduct the current in a material. In free space,

$$\epsilon = \epsilon_0 \approx 8.854 \times 10^{-12} \quad farad/meter$$
$$\mu = \mu_0 = 4\pi \times 10^{-7} \qquad henry/meter$$

3.1.2 The Yee cell

In 1966, Yee initialized a collection of finite-difference equations for time-dependent Maxwell's equations [34]. The mentioned algorithm is a numerical solver which solves both the electric and magnetic fields in time and space analogously. The algorithm simplifies the complex numerical computations to differential equations and tries to find an approximate solution for them. Using both electric and magnetic field for solving the numerical problems give robust results. This method performs the calculations in time domain and due to this principle it covers a wide range of frequencies. As the FDTD method does not use matrixes for computing data, the memory storage consumption is reduced and large number of equations can be solved. In FDTD modelling the computational domain is gridded in Cartesian meshes, where the size of grid cells should be determined precisely to give accurate solution. Although the large computational domain will give more precise solutions, it also requires a very long time which is not desired.

In three-dimensional feature of Yee's algorithm, E and H components are placed in the centre of the grids. Every E-component is surrounded by four H-components. Identically, each H-component is surrounded by four E-components. Figure 3.1-1 shows the one unit cell of Yee lattice with location of different E and H components.
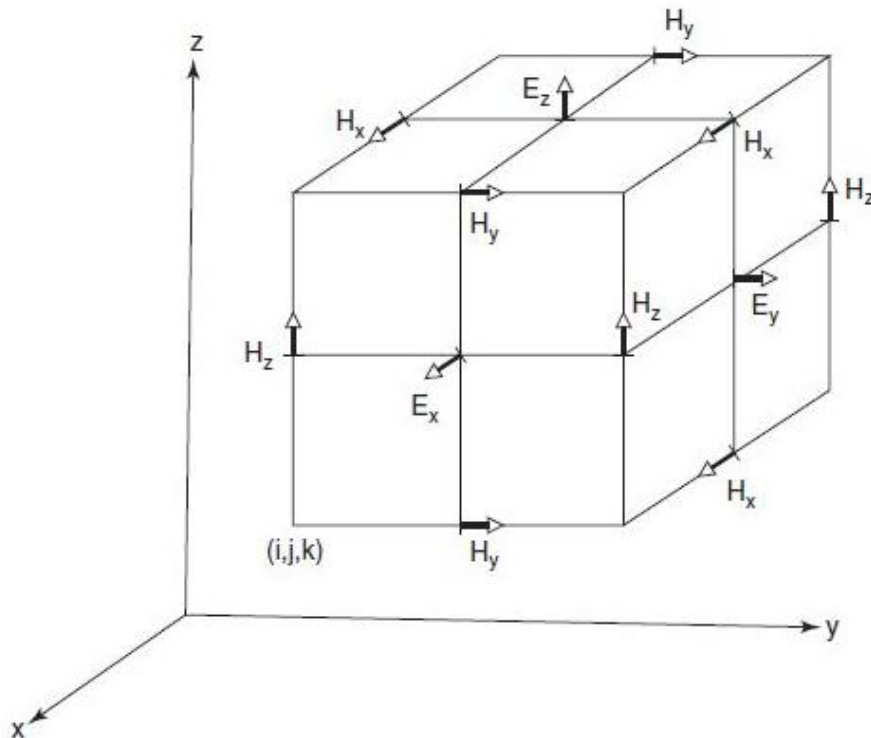

Figure 3.1-1 A Yee space lattice, position of electrical and magnetic field vector components in one unit cell.

The vector components of E-field and H-field of Maxwell's equations are obtained as displayed in the following,

$$\frac{\partial E_x}{\partial t} = \frac{1}{\epsilon}\left(\frac{\partial H_z}{\partial y} - \frac{\partial H_y}{\partial z} - \sigma E_x\right), \qquad (3.1.8)$$

$$\frac{\partial E_y}{\partial t} = \frac{1}{\epsilon}\left(\frac{\partial H_x}{\partial z} - \frac{\partial H_z}{\partial x} - \sigma E_y\right), \qquad (3.1.9)$$

$$\frac{\partial E_z}{\partial t} = \frac{1}{\epsilon}\left(\frac{\partial H_y}{\partial x} - \frac{\partial H_x}{\partial y} - \sigma E_z\right), \qquad (3.1.10)$$

$$\frac{\partial H_x}{\partial t} = \frac{1}{\mu}\left(\frac{\partial E_y}{\partial z} - \frac{\partial E_z}{\partial y}\right), \qquad (3.1.11)$$

$$\frac{\partial H_y}{\partial t} = \frac{1}{\mu}\left(\frac{\partial E_z}{\partial x} - \frac{\partial E_x}{\partial z}\right), \qquad (3.1.12)$$

$$\frac{\partial H_z}{\partial t} = \frac{1}{\mu}\left(\frac{\partial E_x}{\partial y} - \frac{\partial E_y}{\partial x}\right), \qquad (3.1.13)$$

By taking a brief look at equations (3.1.8)-(3.1.10) it can noticed that both H-components are computed from its previous H-components and the most recent E-component. In the same way this procedure can be seen in the equations (3.1.11)-(3.1.13). This process is continued iteratively as long as approaching the maximum simulation time.
Figure 3.1-2 shows the diagram of FDTD time stepping,
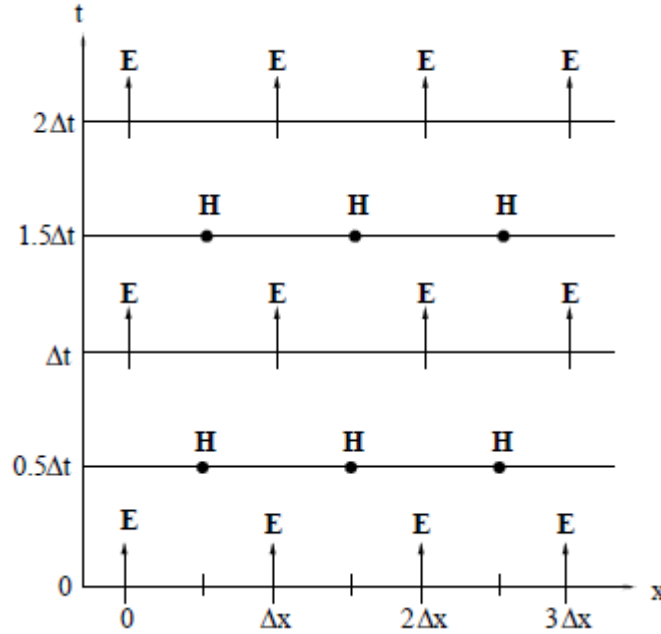
Figure 3.1-2 The FDTD time stepping for E- and H-fields.

Time stepping in FDTD indicate the duration of time that is required for the E- and H-fields to travel from one cell to another. Further, the E-and H-field are computed and updated in each time stepping which is the result of the derivation of simulation time for each grid cell. It was shown that by halving the cell size the accuracy of simulation will be four times better [35].

In FDTD simulation process, the discretization implemented by assigning the integer values of i, j, k in a uniform lattice with the sizes of $\Delta x, \Delta y$ and Δz. This process implies the underneath relation,

$$u_{i,j,k}^{n} = u(i\Delta x, j\Delta y, k\Delta z, n\Delta t) \qquad (3.1.14)$$

Where u is a function of space and n is the nth time step in the iteration phase. So according to these explanations, the equation 3.1.8 can be written as,

$$\frac{E_x|_{i,j,k}^{n+\frac{1}{2}} - E_x|_{i,j,k}^{n-\frac{1}{2}}}{\Delta t} = \frac{1}{\epsilon_{i,j,k}}\left(\frac{H_z|_{i,j,k+\frac{1}{2}}^{n} - H_z|_{i,j,k-\frac{1}{2}}^{n}}{\Delta y} - \frac{H_y|_{i,j+\frac{1}{2},k}^{n} - H_y|_{i,j-\frac{1}{2},k}^{n}}{\Delta z} - \sigma_{i,j,k} E_x|_{i,j,k}^{n}\right) \qquad (3.1.15)$$

Similarly, time stepping can be written for the rest of the equations.
To obtain numerical stable FDTD solution [36], Δt should satisfy the following requirement,

$$\Delta t \leq \frac{1}{\sqrt{\frac{1}{(\Delta x)^2} + \frac{1}{(\Delta y)^2} + \frac{1}{(\Delta z)^2}}} \qquad (3.1.16)$$

If the shape of the lattice is chosen to be cubic, then the size of the spatial steps will be equal, i.e. $\Delta x = \Delta y = \Delta z = \Delta$. Hence, the condition of numerical stability can be simplified as,

$$\Delta t = \frac{\Delta}{c\sqrt{3}} \qquad (3.1.18)$$

3.2 Electromagnetic Source Modelling

In the FDTD simulation, an electromagnetic wave source should be specified to describe the propagation of signals as accurately as possible. For this purpose, there are two different source modelling.

3.2.1 Hard source Modelling

In most of FDTD simulations hard source is applied as source modelling because it is easy to implement. In the case of sampling the transmitters with hard source, E-field strength is specified at the desired position and surrounding E-fields are modelled according to the effects from antennas at the receiver positions [37]. Transmission and reflection parameters are obtained from the propagation of electromagnetic waves through the targeted object. The reflection signal will return to the source point after the defined time step [38].

3.2.2 Thin Wire Modelling

In 3D FDTD simulation's algorithm, there is a need for more realistic antenna modelling. Thin wire approximation provides this possibility to model monopole antennas. In this case, according to the Ampere's law the transmitter antenna carries the current through the FDTD domain until it reaches the closest H-field components [39]. In our experiment setup the antennas have been modelled as thin wire. This modelling containing Perfect Electric Conductor (PEC) which corresponds to electrical field where all tangential components set to zero [17]. In addition, resistive voltage source (RVS) of 50 Ω has been chosen for impedance values to feed at the transmitter, receiver and inactive antennas locations. The reason of using RVS is to remove the reflected problem, which exists in hard source modelling, in the source point.

3.3 Absorbing boundary condition

The E- and H-field components are computed in the all cell grids in the computational domain. In the FDTD simulation the chosen computational domain is finite. Therefore, absorbing boundary is introduced in the FDTD modelling. It should be kept in mind that describing these boundaries may cause some errors which should be minimized to achieve more realistic simulations. The major consideration in FDTD is how to terminate the grids and absorb outgoing waves. To this end, a layer of PEC boundary is defined which doesn't need a lot of memory to be implemented. This is what happens if the FDTD equations are implemented straight forward and there is no need to add extra PEC. In this scheme, the parallel E-fields in the boundary is equal to zero. The drawback of this method is the reflection from the wall of conductor which is not desired. One solution for compensating this deficiency is assuming a larger space for wave propagation within the computation domain when the background medium is supposed to be lossy. However, this may cause increment in the computation time and memory consumption.

In 1981, Mur [40] originated the first numerically stable absorbing boundary condition (ABC), which can be utilized both for two- and three-dimensional configurations. In ABC an infinite and unbounded computational domain is defined. As the ideal computation domain is considered to be in open space, Mur simulated unbounded surrounding shortening the grids and assuming the absorbing boundary condition at its artificial boundaries located outside of the original computational domain. Care should be taken as the reflection will be increased in the case of skew collisions and this increment has straightforward relation with the increase of the collision angle.

Berenger developed a technique for absorbing electromagnetic waves without reflection, where the plane and wave's propagation should be perpendicular at the boundaries [41].The principle of this technique is relied on splitting the E-and H-field components into two perpendicular components in the absorbing boundary region, called perfectly matched layer (PML). Moreover, by utilizing this method which is described for two dimensional problems, any kind of electromagnetic waves can propagate in the boundaries and absorbed finally. Katz et al. implemented this technique in three dimensional case, discussed in [42].

There are different novelties for PMLs. In this master thesis, Convolutional PML (CPML) is introduced to absorb electromagnetic waves in the boundaries which is known as the most acceptable techniques recently [43]. In this method, the E and H components don't need to be split anymore. Moreover, this procedure is known as most efficient technique for PML due to reducing memory consumption and also absorbing plane waves.

3.4   Antenna Modelling

As mentioned before, in the experimental prototype monopole antennas are used due to their simplicity to model and construct. Monopole antennas are a special kind of dipole antennas. They are one half of a dipole antenna and also known as resonant antennas. The resonant frequency, is chosen according to the interested frequency span in the measurement set up. The most popular form of monopoles is quarter-wave monopole in which the length of antenna is determined as

$$l = \frac{\lambda}{4} \qquad\qquad (3.3.1)$$

Where λ is,

$$\lambda = \frac{v_p}{f_r} \qquad\qquad (3.3.2)$$

In equation (3.3.2), f_r is the resonance frequency at which the antenna has the best performance and v_p represents the phase speed values in the medium and is defined as

$$v_p = \frac{c}{\sqrt{\epsilon_r}} \qquad\qquad (3.3.3)$$

Where c, is the speed of light in the vacuum and ϵ_r, is the relative permittivity of the medium [44], [45].

Bearing in mind that, there is a need of defining a precise length of antenna to increase the accuracy of reconstruction image.

Since it is not possible to get accurate models of 3D wave propagation of the real world antennas in a 2D model, there is essential need to introduce a 3D wave pattern. A 3D algorithm is described to be used with this measurement set up. The mentioned 3D algorithm, is applicable to model accurately antenna and wave propagation. This will be discussed in more details in section 4. In our experimental prototype, the antenna arrays are mounted in a cylindrical pattern on a tank. The position of antenna arrays are designed in 3D space. The antenna arrays include 24 monopole antennas in total. In each array there are 8 antennas where rotated by 22.5 degree to position of antennas in the other array. Also, each ring has 40 mm height apart from the other ring. The configuration is designed in three circles with eight antennas in each array. The Figure 3.4-1 illustrates the designed antennas position.
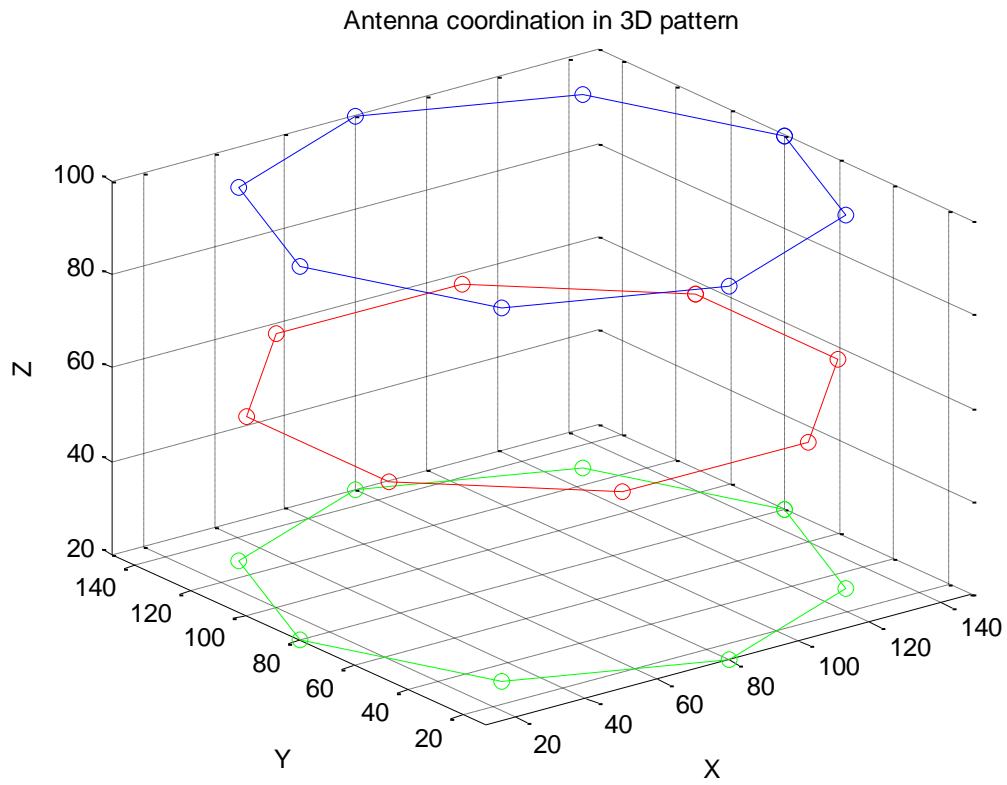
Figure 3.4-1 The configuration of designed antenna arrays in 3D pattern

4 Image Reconstruction Process

This part will give brief information about the principles of tomography. Then, the features of inverse scattering problem and its solutions are discussed. Finally the utilized image reconstruction algorithm is explained.

4.1   Definition and features of inverse scattering problem

The fundamental of tomography technique is creating cross sectional images of an object. The concept of this non-invasive method is reconstructing the interior structure of an object by evaluating the measurements have done by illuminating the target object from several angles. The obtained image represents the mathematical model of the data which is measured by the system. Afterwards, there is a need for a mathematical operation named inversion, to make the acquired data understandable for analysing. According to previous explanations the principle of image reconstruction in MWT is solving the inverse problem of scattering data which are measured with antennas around the object. To achieve this goal, the acquired error between the scattering electric fields and measurements from computational numerical simulation should be as small as possible to obtain a high resolution image of the target. The resolution and accuracy of an image are highly important aspects in the reconstruction process. Resolution of an image indicates the number of pixels in the image; consequently high resolution images includes small pixel sizes. Beside this, accuracy of an image depends on the precise estimation of dielectric properties of living tissues and should be taken in account while modelling and calibrating the system.

The forward or direct problem is computing the electromagnetic waves that are propagated along a given object and the inverse problem is to determine the shape of the object according to the scattered waves from the object. It is clear that a 3D high resolution image with precise dielectric properties is very complex and requires intensive computational effort.

To explain the inverse scattering problem, it is necessary to describe two conditions of the problem: well and ill-posed problem.

Hadamard, [46], states that in well-posed problems there is a solution for each problem (existence) and this solution is unique and depends continuously on data (stability). Inverse problems are usually known as ill-posed problems. In the case of this master thesis, it is because of restriction in the number of antennas which gives limited samples. In addition the problem can't be stable, because any small change in measurement field will make a sensible change in the solution and due to this fact, there is not unique solution for the problem. To get rid of ill-possedness of a problem reconstruction methods such as Born iteration (BIM) and Distorted Born iteration (DBIM) can be used. These methods apply the distorted Green's function and upgrade it in each iterative optimization [47], [48]. In this work, conjugate gradient [49], is utilized as a local optimization method.

Advanced computer resources are required to compute complex nonlinear approximation and image reconstruction in real time.

4.2 Three dimensional image reconstruction algorithm

Different type of reconstruction algorithms can be performed for reconstructing the objects with low and high contrast in dielectric properties. For low contrast cases, linear approximations such as the Born and Rytov approximations [50], [51], known as fast reconstruction algorithms, can be used. While the story in high contrast objects is different. In addition, it was confirmed that the performance of mentioned linear approximations is high enough when the target is small and the contrast between backgrounds is the less However this is not the case for biological tissues, as studied in [52],[53]. Objects with high contrast dielectric properties need another alternative because the permittivity and conductivity values are non-linearly dependent from the measured E-field of receiving antennas. In addition, to obtain more accurate reconstruction results iterative algorithms should be considered.

In this work an iterative electromagnetic time domain inversion algorithm is utilized to reconstruct dielectric parameters of one or several objects. The basis of this method is originating from FDTD simulation of electromagnetic problems. As discussed previously, to figure out the gradients which are used in optimization algorithm, it is necessary to compute the adjoint Maxwell problem.

The concept of image reconstruction in this work is based on measuring the scattering parameters which are produced via the transmitter and receiver antennas and comparing the measured data with numerical simulation of the system. This operation is performed iteratively and reconstruction is terminated when the minimum difference possible is achieved and dielectric parameters are updated.

To carry out the reconstruction procedure, a cost function is defined. The idea behind the reconstruction algorithm here is minimizing the difference between the simulated and measured electric field in the cost function. The difference is minimized by changing the dielectric properties and as a consequence of this process the simulated fields change as well. This change should be done in order to approach the measured field. Ideally, if a perfect reconstruction is done, the difference between the measured and simulated fields should be zero. The goal here is to make this difference zero, to obtain the desired and most accurate reconstruction results. This minimization is accomplished by computing the gradients. The gradients are computed performing the FDTD simulation of electromagnetic problem and combining the result of this simulation with the solution of the adjoint Maxwell's equation. In this process, an initial guess is made about the dielectric properties of the target object and this prediction is updated at each iteration.

The aim of reconstruction process is to minimize the given cost function,

$$F(\epsilon, \sigma) = \int_0^T \sum_{m=1}^M \sum_{n=1}^N \left(|E_{mn}^{sim}(\epsilon, \sigma, t) - E_{mn}^{meas}(t)|^2 \right) dt \qquad (4.2.1)$$

Where, $E_{mn}^{sim}(\epsilon, \sigma, t)$ denotes the simulated electric field from the computational model with M and N values representing the number of transmitter and receiver antennas respectively. In addition, $E_{mn}^{meas}(t)$ is time varying electric field and acquired by computing the inverse Fourier transform of the measured electrical field, $E_{mn}^{meas}(f)$.

The conjugate gradient algorithm [49] is used to minimize the function value. In the mentioned algorithm the gradients are derived by evaluating the increment of the

permittivity $\epsilon + \delta\epsilon$ and conductivity $\sigma + \delta\sigma$ and the amount of change in the function that is derived according to perturbation analysis.

The following shows how the function can be represented by Fréchet derivative,

$$F'(\epsilon, \sigma) = \langle G_\epsilon(x), \delta_\epsilon \rangle + \langle G_{\sigma/<\sigma>}(x), \delta_\sigma \rangle \qquad (4.2.2)$$

Where, the result of the inner product represents the surface integral of the reconstruction domain,

$$\langle G_i(x), \delta_i(x) \rangle = \iint_S G_i(x)\delta_i(x)\, dS \qquad (4.2.3)$$

According to what has been discussed previously, the source for solving Maxwell's adjoint equations is obtained by computing the differences between measured and simulated electrical fields. The gradients in each grid point can be computed by using the mentioned difference and can be written as

$$G_\epsilon(x) = 2 \sum_{m=1}^{M} \int_0^T \tilde{E}_m(\epsilon, \sigma, x, t). \ \partial_t E_m(\epsilon, \sigma, x, t) dt \qquad (4.2.4)$$

$$G_{\sigma/\langle\sigma\rangle}(x) = 2\langle\sigma\rangle \sum_{m=1}^{M} \tilde{E}_m(\epsilon, \sigma, x, t). E_m(\epsilon, \sigma, x, t) dt \qquad (4.2.5)$$

Where, $\tilde{E}_m(\epsilon, \sigma, x, t)$ is the simulated electrical field as the solution for the adjoint problem when m is the number of the transmitter antenna (defined as source) and $E_m(\epsilon, \sigma, x, t)$ denotes the numerical computed electrical field in the reconstruction domain.

While computing the gradients, some differences can exist in the scaling process and this is due to the different values of permittivity and conductivity. Defining a scaling parameter, $\langle\sigma\rangle$ is an a possibility to remedy this phenomenon, which is given as,

$$\langle\sigma\rangle = \left(\int_0^\infty \sum_{m=1}^{M} \sum_{n=1}^{N} \left|\hat{E}_{mn}(\omega)\right|^2 d\omega \right)^{-1}$$
$$\times \left(\int_0^\infty \sum_{m=1}^{M} \sum_{n=1}^{N} \left|\hat{E}_{mn}(\omega)\right|^2 \omega d\omega \right) \qquad (4.2.6)$$

In this formulation, $\hat{E}_{mn}(\omega)$ is the Fourier transform of measured electrical field, M and N are the number transmitter and receiver antennas respectively. It should kept in mind that determining the scaling factor plays an important role in performance of the set up system and achieving the desired results for reconstruction.

In reconstruction process, after updating the gradients employed in conjugate algorithm, a line search method known as parabolic interpolation is done in negative direction to detect the minimum value for the objective functional parameter. In this work, a regularization technique is performed to transform the ill-posed inverse

problem to well-posed problem. Also, a low pass filter is applied to get rid of undesired signals in the measurement and create smoothing condition on the reconstruction process.

4.3 Calibration of data

The calibration of the measurement and simulated data are an important aspect. The calibration procedure for the simulated data is introduced in the following,

$$E_{cal}^{meas}(f) = \frac{S_{scat}^{meas}(f)}{S_{ref}^{meas}(f)} E_{ref}^{sim}(f) \tag{4.3.1}$$

Where $S_{scat}^{meas}(f)$ indicates the measured transmission and reflection coefficient performed by antenna combination on the target object and $S_{ref}^{meas}(f)$ are the measured S-parameters of the empty system. Finally, $E_{ref}^{sim}(f)$ corresponds to the reference electrical field which is obtained by taking the inverse Fourier transform of the Gaussian pulse with a certain frequency$w$, and can be written as

$$E_{ref}^{sim}(t) = E_0 \exp\left(-\frac{1}{2}\frac{(t-t_1)^2}{t_0^2}\right)\sin(wt) \tag{4.3.2}$$

As mentioned already, the pulse used in this time domain algorithm is a Gaussian pulse, with a certain centre frequency, f_c, and a certain full width half maximum (f_FWHM). According to this definition, the frequency span of the pulse is specified from $f_c -$ FWHM to$f_c +$ FWHM. The frequency components of the measurement system should be thus set to operate in the mentioned frequency span.

As a consequence of this calibration, $E_{cal}^{meas}(f)$ is calculated and is used in equation (4.3.1) to compare with the simulated electric field.

Besides, to eliminate the artifacts in the proximity of antennas, the radius of the reconstruction domain assumed to be smaller than antenna arrays and also attenuated the gradients close to the boundary of the reconstruction domain. To this end, the gradients can be multiplied by the following formulation [17],

$$1 - \exp[-0.15(R_{rd} - r)^2] \tag{4.3.3}$$

Where, R_{rd} is the radius of reconstruction domain and r denotes the radial distance from the centre of the domain.

4.4 Summary of 3D image reconstruction procedure

First of all the gradients are computed according to (4.2.4) and (4.2.5), afterwards the threshold value is defined to find the target objects in reconstruction domain. Further, new gradients are computed again with the same equations (4.2.4) and (4.2.5). The obtained new gradients are used to optimize the position and size of the target object. This process is iteratively accomplished until all objects are detected and then reconstruction is terminated.

5 Measurement procedure

The following is a detailed description of experimental prototype and several devices that are utilised for evaluating the simulation data.

5.1 Vector Network analyzer (VNA)

In the experimental process, a Vector Network analyzer (VNA), has been utilized to measure the scattering parameters. The measurement procedure has been performed by evaluating the magnitude and phase of scattering parameters. The output of the system are frequency domain signals, hence the system utilizes the inverse Fourier transform to give time domain signals Figure 5.1-1 shows the VNA device which has been used to perform measurements in the laboratory.
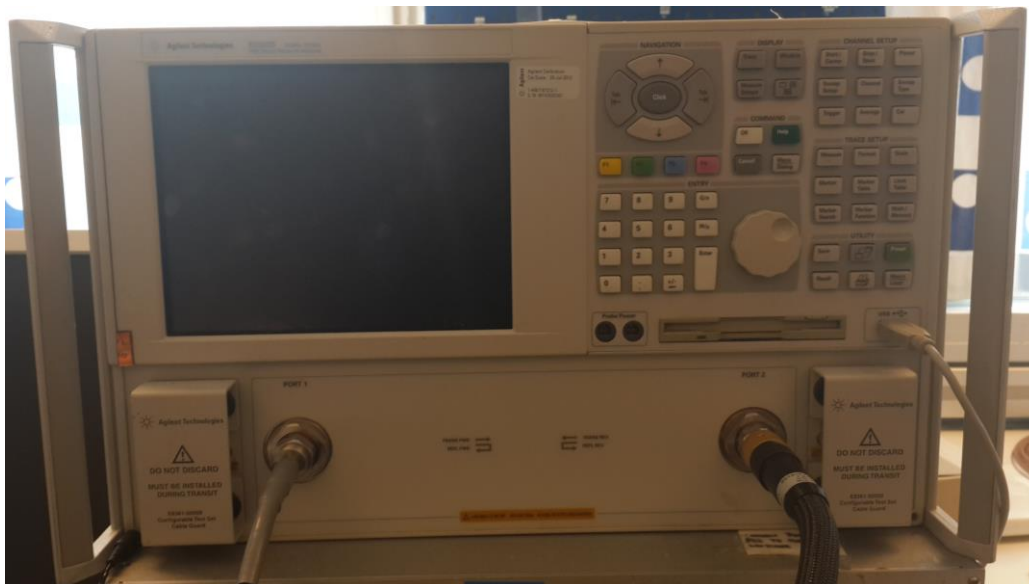

Figure 5.1-1 The network vector analyzer Agilent E8362 B, used to perform measurements.

5.2 Measuring process and S-parameters

VNA includes two ports: one is employed for sending the signal and the other one is receiving it simultaneously.

As displayed in Figure 5.2-1 two types of measurement are done with VNA system: forward and reverse measurement.
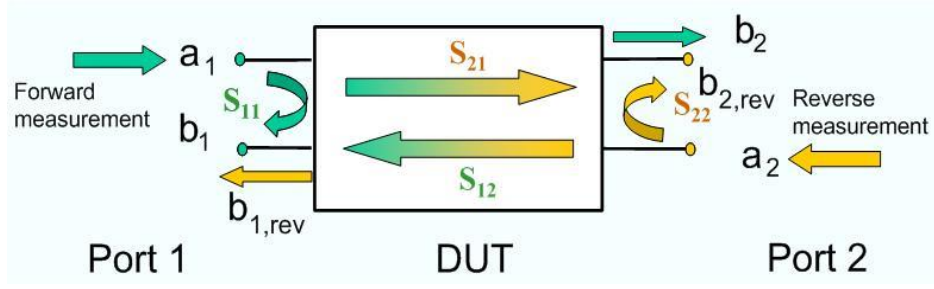
Figure 5.2-1 Scattering parameters of a two –port network

In the forward measurement, the signals are leaving port 1, while in the reverse measurement the signals are leaving port 2. If the signals propagate from one port and are reflected back to the same port, it is called a reflection measurement. Otherwise, if the signal leaves one port and is transmitted to the other port, it is assumed as transmission measurements.

The relation between the incident and reflected wave can be written as,

$$\begin{pmatrix} b_1 \\ b_2 \end{pmatrix} = \begin{pmatrix} S_{11} & S_{12} \\ S_{21} & S_{22} \end{pmatrix} \times \begin{pmatrix} a_1 \\ a_2 \end{pmatrix} \qquad (6.1.1)$$

Where four different scattering parameters of two-port system are described as,

$$S_{11} = \frac{b_1}{a_1} \mid_{a_2=0} \quad \& \quad S_{21} = \frac{b_2}{a_1} \mid_{a_2=0} \qquad (6.1.2)$$

$$S_{12} = \frac{b_1}{a_2} \mid_{a_1=0} \quad \& \quad S_{22} = \frac{b_2}{a_2} \mid_{a_1=0} \qquad (6.1.3)$$

The following list describes the abbreviation of S-parameters:

- S_{11} denotes the forward reflection in which the signal is propagated from port 1 and reflected back to port 1.
- S_{21} denotes the forward transmission in which the signal is propagated from port 1 and transmitted to port 2.
- S_{12} denotes reverse transmission in which the signal is propagated from port 2 and transmitted to port 1.
- S_{22} denotes reverse reflection in which the signal is propagated from port 2 and reflected back to port2.

S parameters are voltage ratio and have no units in SI system. The magnitude of the S-parameters in dB can be written as,

$$S_{ij}(dB) = 20 * \log[S_{ij}(magnitude)] \qquad (6.1.4)$$

Where i is the output and j is the input (excited) port. Furthermore, by loading the measured S-parameters in MATLAB for each frequency, real and imaginary part of S-parameters are calculated and results are plotted.

Two different length for monopole antennas have been simulated. In the first case, the thin wire model has the length of 9 mm and radius 0.2 mm. Figure 5.2-2 represents two selected sets of S-parameters, S11 and S12 of simulation data when a single object of

sunflower oil has been located in the centre of simulation space. As seen, the plotted S12 implies very low amplitude.

In the second case, which will be described in section 6.2.2, the S-parameters of simulation and corresponding measurement data of a cup of sunflower oil will be illustrated and discussed more in details where the length and radius of the monopole antenna have been chosen as 20 mm and 0.5 mm representing the same sizes in the existent setup system.
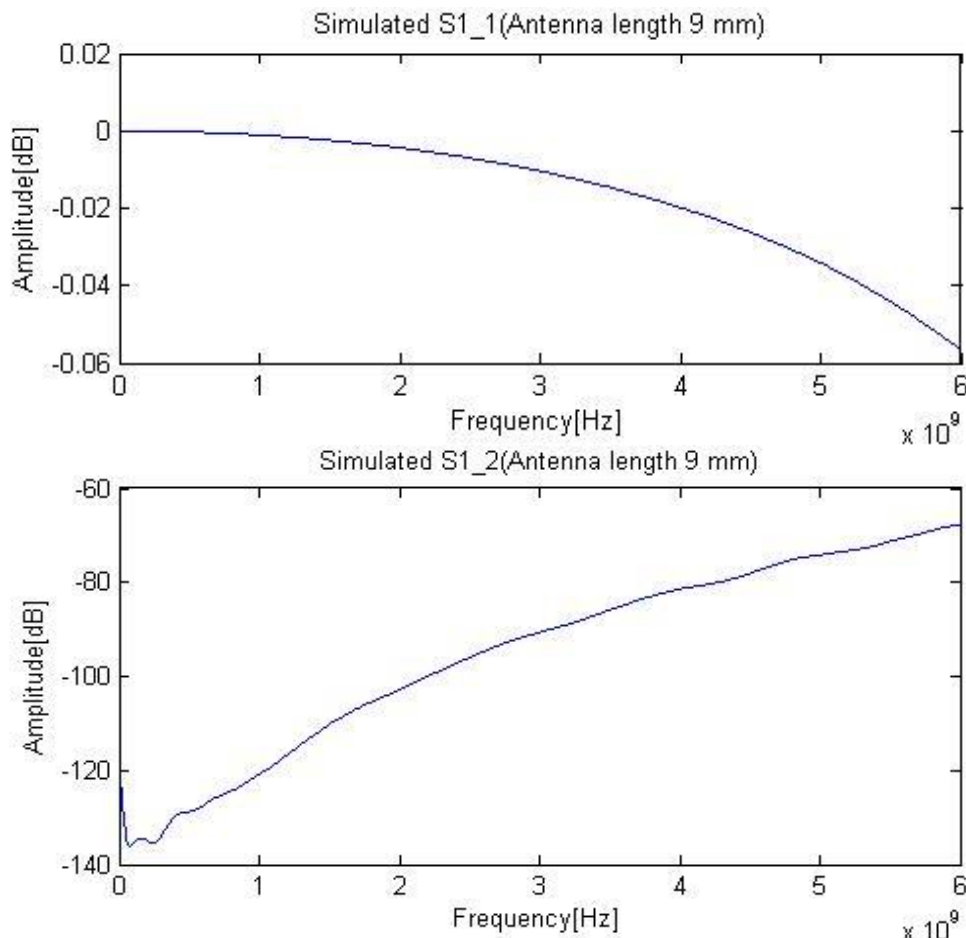

Figure 5.2-2 Simulated S1_1 and S1_2 parameters with antenna length of 9 mm and radius 0.2 mm

S11 parameter indicates the voltage reflection coefficients that describes the efficiency of an antenna. The resonance frequency describes the minimum reflection in defined frequency. If the reflection coefficient of an antenna is -10 dB and -3 dB of the power is received by another antenna, then -7 dB is reflected power. Values of S11 less than -10 dB imply good performance of the antenna.

5.3 Electronic Calibration Module

Agilent/HP 85093C RF Electronic Calibration Module, briefly ECal module, has been used for calibrating the vector network analyzer as illustrated in Figure 5.3-1. The device involves an accurate single connection calibration technique to calibrate the VNA system as fast as possible. This module applies a full two-port calibration and contains unique values for S-parameters which are stored in the memory of the module. While measurements are performed, the module conducts the S-parameters to VNA for

calibration and computing the present errors in VNA. In addition, VNA system takes the calibrated data in the desired frequency span as input signal. Consequently, the calibration process is performed at the output of the switching matrix according to the specified start and stop point for frequency components, number of measurement points and IF bandwidth.

Figure 5.3-1 Electronic calibration module Agilent/HP 85093C, utilized for calibrating vector network analyzer

5.4   Switching multiplexer

Another device is a 2:32 computer controlled microwave switching multiplexer system called CYTEC CXM/128-S-W. The function of this apparatus is connecting and disconnecting the transmitter and receiver antennas to VNA automatically. As displayed in Figure 5.4-1 , 24 coaxial cables connect antennas to VNA and multiplexer for measurement process.
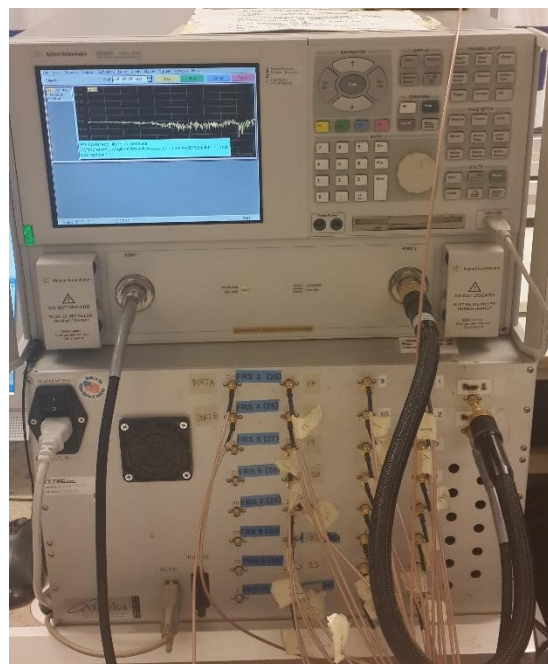

Figure 5.4-1 The switching matrix connected to VNA

5.5 Antenna arrays prototype

As discussed beforehand, a cylindrical antenna array mounted on a tank has been used as main part of the measurement setup, as shown in Figure 5.5-1. The tomographic measurement is performed with one of the antennas as transmitter at time, and the rest of antennas acting as receivers to measure the scattered signals (radiation). This procedure is repeated until all of antennas operate as transmitter which leads to large amount of measurement data for 3D reconstruction algorithm.
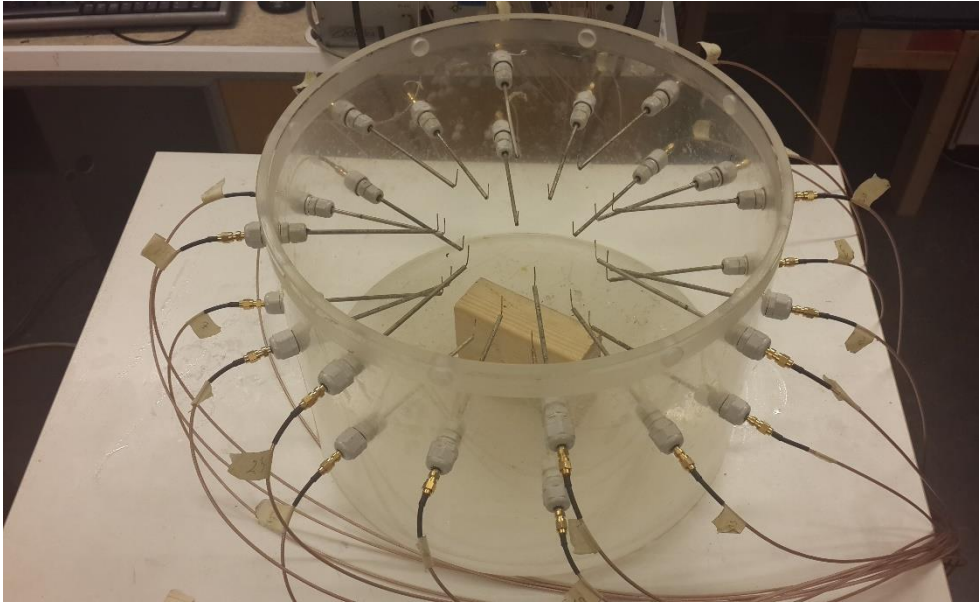

Figure 5.5-1 The set up system designed with 24 monopole antenna in cylindrical pattern.

In this set up the radius of the cylindrical antenna is 70 mm, and it can easily be changed in order to have large or small measurement domain. The height of the plastic tank is 275 mm, the length of the monopole antennas is 120 mm and their radiating elements have the height of 20 mm and radius 0.5 mm. Figure 5.5-2 to Figure 5.5-4t shows the imaged object, measurement antenna and whole measurement setup which have been used to perform microwave measurements in this master work.
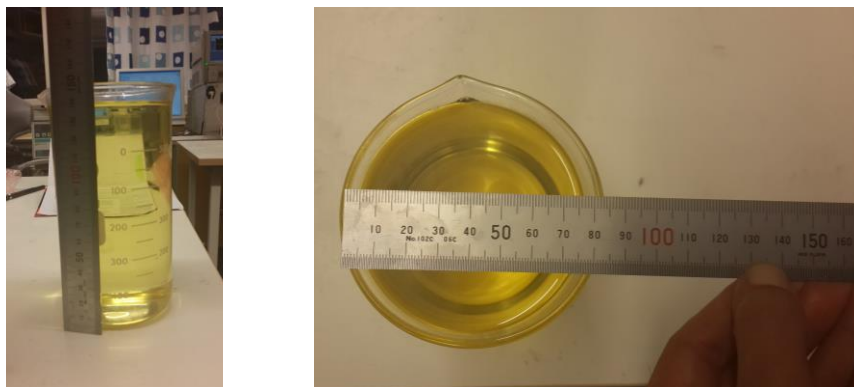

Figure 5.5-2 The view of imaged object

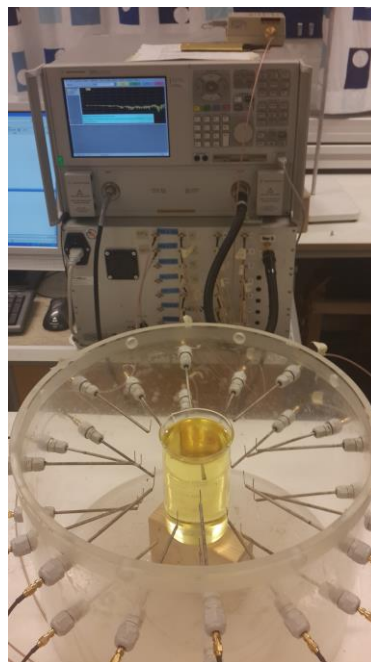*Figure 5.5-3 The view of measurement antennas length*

Figure 5.5-4 The measurement system connected to VNA including target object

6 Results and Discussion

In this chapter the results of the simulations and measurements including different objects with different sizes and frequency contents are described in more details.

6.1 Experimental Configuration

As mentioned in previous chapter, the experimental setup has been utilized to perform measurements. To this end a single object made from sunflower oil with dielectric properties $\epsilon_r = 2.7$ and $\sigma = 0.015$ S/m at frequency 3.0 GHz has been used to simulate a fatty breast tissue as shown in Figure 6.2-1. The target object is in cylindrical shape whereas the radius of cylinder is 40 mm and the height is 140 mm. It has been located in the 20 mm offset in the x and y directions from the central domain of antenna arrays to minimize the effect of antennas artefacts in the reconstructed images.

It should be taken into consideration that although the higher frequency implies good resolution images but it has less depth of penetration. Therefor the centre frequency has been set to 3.0 GHz with full width half maximum (FWHM) 3.0 GHz.

Another important parameter is simulation time which has to be selected accurately. It should be long enough to make the transmitted pulses be able to propagate in the simulation medium and to reach to zero at the end of the process. The value for simulation time changes according to selected frequency and it is in the range of Nano seconds. In addition the measured data needs to be checked before running the reconstruction. To this end, the measurement data is plotted in MATLAB to ensure that the data doesn't contain error, as shown in Figure 5.2-3 and Figure 5.2-4.

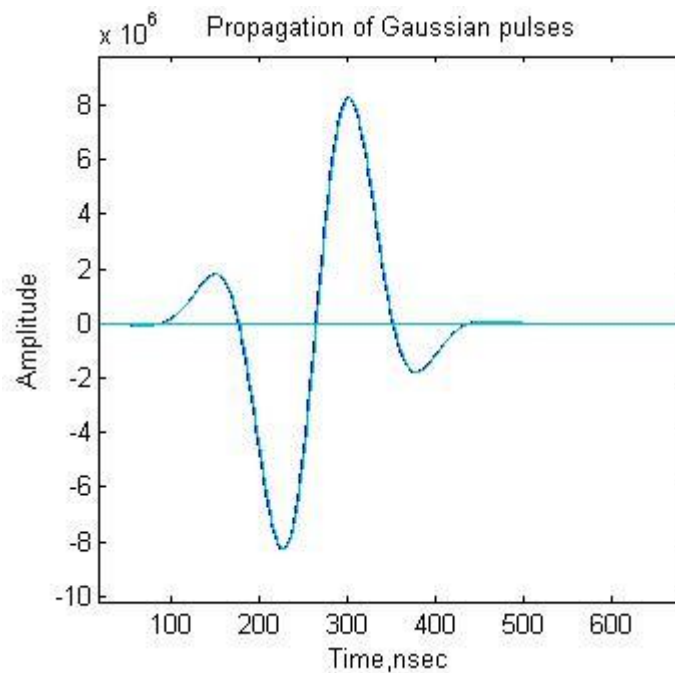Figure 6.1-1 illustrates the propagation of pulses in the medium.

Figure 6.1-1 The propagation of Gaussian pulse in the medium

6.2 Reconstruction of one single Object in different mediums

In this part, the measurement and simulation of a cup of sunflower oil have been performed in different positions, background medium and frequency components. The reconstructed images and the setting of reconstruction algorithm have also been discussed.

6.2.1 Simulation of a cup of sunflower oil with air as background

To avoid the antennas artifact and reconstruction errors, the antennas should be placed outside of the reconstruction domain. Therefore, the 3D reconstruction domain is simulated as a cylindrical volume with radius of 60 mm and height of 120 mm. In the simulation and reconstruction process monopole antennas have been used with the length of 20 mm and diameter of 0.5 mm according to setup system. In all of the simulation cases, the forward calculations have been made on 1 mm grid cell size. As the reconstruction process requires a large time and memory usage, a parallel Linux cluster with 32 cores and 2 nodes has been used to run the code.

The FDTD modelling and setting of reconstruction algorithm are summarized in Table 6.2-1.

Table 6.2-1 3D FDTD modelling and reconstruction parameter setting for a single object in the system with air as background

FDTD spatial grid	$160 \times 160 \times 160$
Grid cell size (in x, y and z direction)	1 mm
Number of CPML	11
Simulation time	4.0×10^{-9} sec
Source function	Gaussian envelope sinusoidal function
Source centre frequency	3.0 GHz
Source FWHM bandwidth	3.0 GHz
Antenna model	Thin wire monopole
Feed model	50 Ω RVS
Background (air)	$\epsilon_r = 1.0$, $\sigma = 0.0$ S/m

After completing the reconstruction process, results of the reconstructed permittivity and conductivity have been obtained. The derived files contain matrices corresponding of the grid cell size dimension, space length and number of iterations. In all of the acquired results the last iteration of the reconstructed images have been selected to evaluate the permittivity and conductivity of the modelled objects.

Figure 6.2-1 is an overview of whole object and representing the full reconstruction domain of simulated data with cross sections in the centre of the objects. Figure 6.2-2 and Figure 6.2-3 illustrate the 2D images of the objects in x-y plane and five different heights have been chosen to give clear and understandable illustration of the reconstructed images.
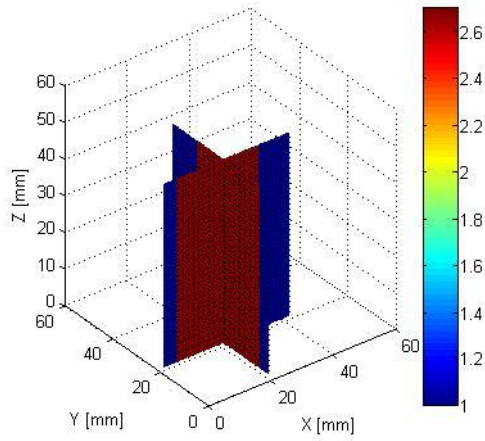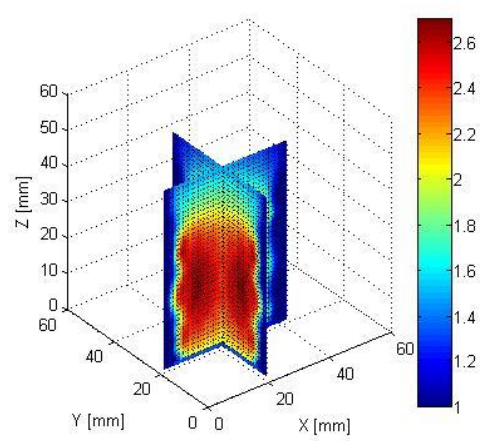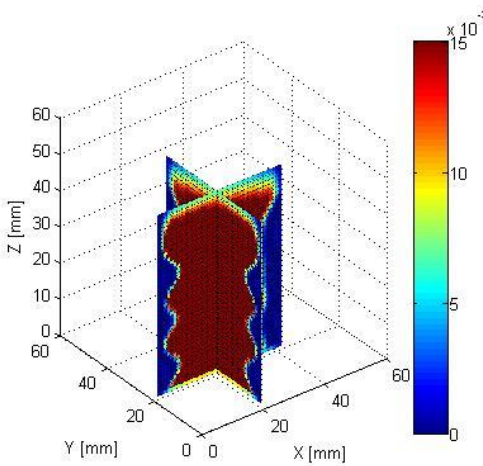
(a)   Original ϵ_r model   (b) Reconstructed ϵ_r for simulated data at 1.0 GHz
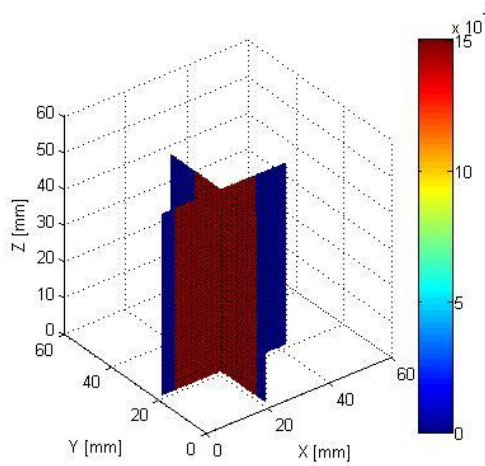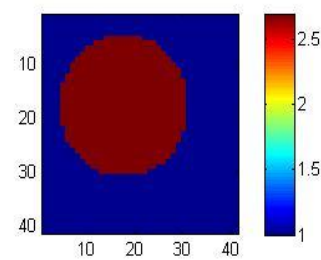
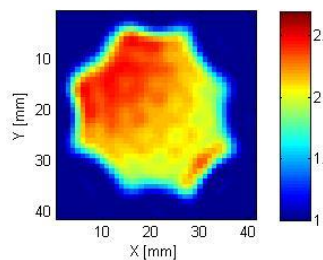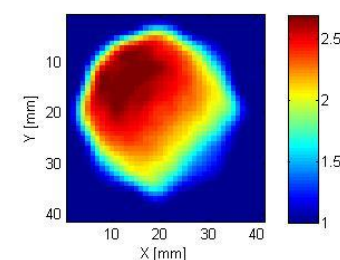(c)   Original σ model   (d) Reconstructed σ for simulated data at 1. 0 GHz

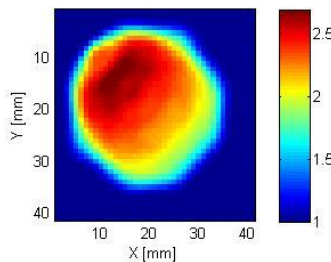*Figure 6.2-1 3D representation of the original model and simulated reconstruction*
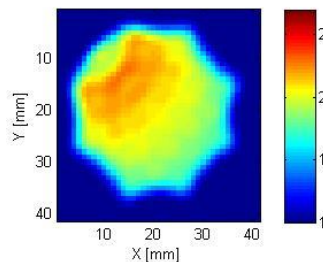

(a)   Original permittivity   (b) Reconstructed ϵ_r, z = 8   mm   (c) Reconstructed ϵ_r, z = 16   mm

(d) Reconstructed ϵ_r, z =24 mm   (e) Reconstructed ϵ_r, z = 32 mm   (f) Reconstructed ϵ_r, z = 40 mm

Figure 6.2-2 2D representation of reconstructed images of the single target object using accurate antenna modelling.
(a) is the original model of permittivity. (b)-(g) Reconstructed permittivity images of simulated data with 5 iteration
are shown in different heights using centre frequency and FWHM 1.0 GHz

(a) Original conductivity   (b) Reconstructed σ, z = 8 mm   (c) Reconstructed σ, z = 16 mm

(d) Reconstructed σ, z =24 mm   (e) Reconstructed σ, z =32 mm   (f) Reconstructed σ, z =40 mm
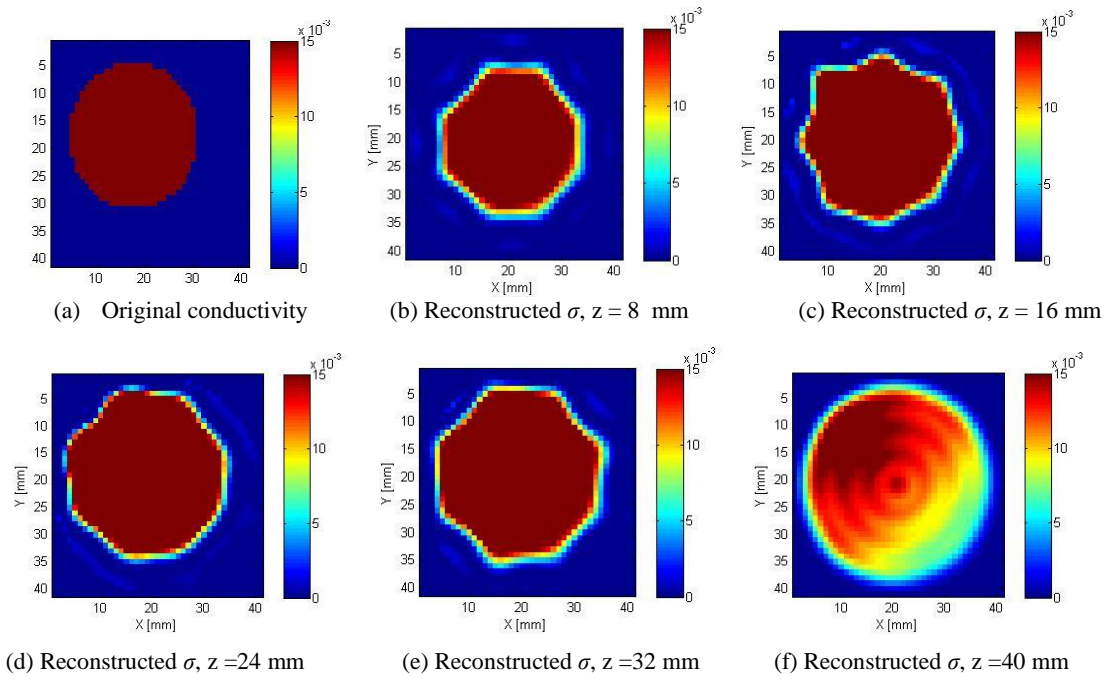
Figure 6.2-3 2D representation of reconstructed images of the single target object using accurate antenna modelling. (a) is the original model of conductivity. (b)-(g) Reconstructed conductivity images of simulated data with 5 iteration are shown in different heights using centre frequency and FWHM 1.0 GHz

The 2D representation in x − y plane has been selected to indicate the results. The forward FDTD calculation has been made on 1 mm grid cell size in x, y and z directions, and the inverse calculations have been performed on 3 mm. The reconstructed images have been reshaped to be in the scale of 3 mm, as illustrated in Figure 6.2-1. Also, the dielectric distribution of the object is completely clear in each of five different z − heights. Five iterations have been made and reconstruction process took about 3 hours to run the inverse calculation for simulated data. In this case, the reconstruction algorithm is using a centre frequency 1.0 GHz with a FWHM 1.0 GHz.

The large object has been resolved successfully. However, reconstruction was not converged completely. So the reconstruction process has been set to 10 iterations instead of 5 in the following simulation.

(a) Original ϵ_r model   (b) Reconstructed ϵ_r for simulated data at 1.0 GHz

(a) Original σ model

(b) Reconstructed σ for simulated data at 1.0 GHz

Figure 6.2-4 3D representation of the original model and simulated reconstruction

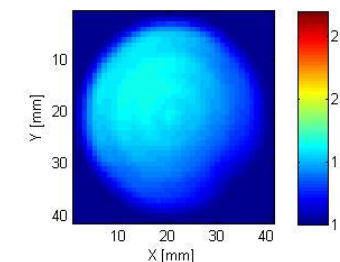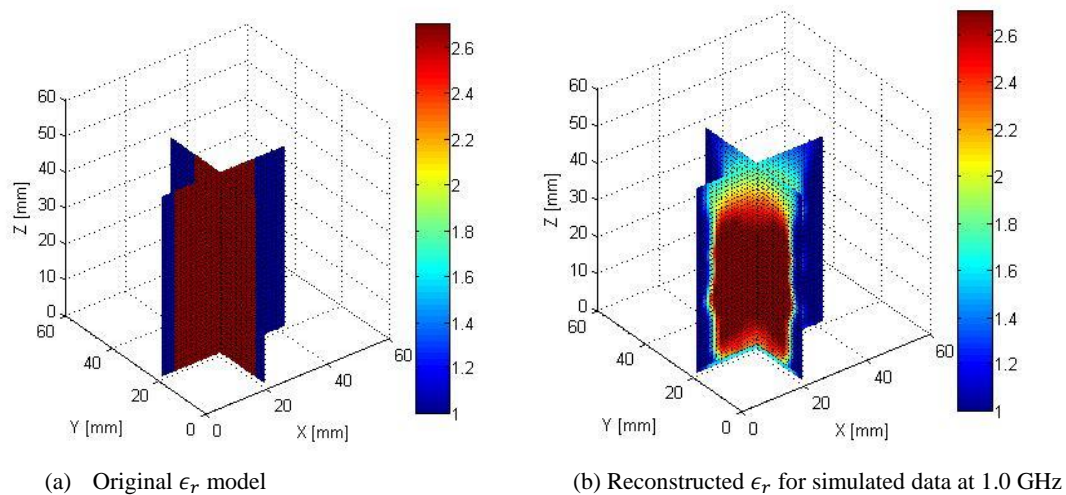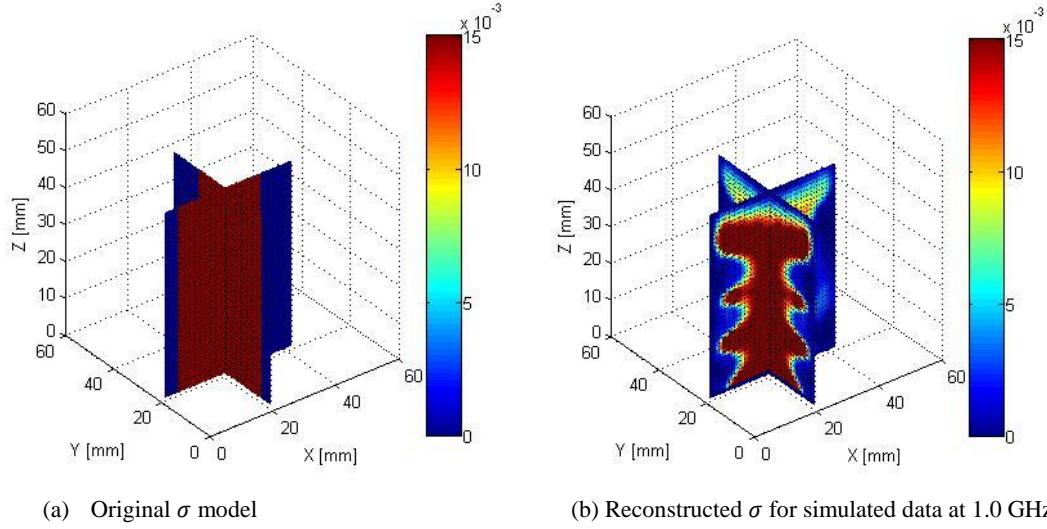(a)   Original permittivity

(b) Reconstructed ϵ_r, z = 8 mm

(c) Reconstructed ϵ_r, z = 16 mm

(d) Reconstructed ϵ_r, z = 24 mm

(e) Reconstructed ϵ_r, z = 32 mm

(f) Reconstructed ϵ_r, z = 40 mm

Figure 6.2-5 2D representation of reconstructed images of the single target object using accurate antenna modelling.
(a) is the original model of permittivity. (b)-(g) Reconstructed permittivity images of simulated data with 10 iteration
are shown in different heights using centre frequency and FWHM 1.0 GHz

(a)   Original conductivity

(b) Reconstructed σ, z = 8 mm

(c) Reconstructed σ, z =16 mm

(d) Reconstructed σ, z = 24 mm   (e) Reconstructed σ, z = 32 mm   (f) Reconstructed σ, z =40 mm
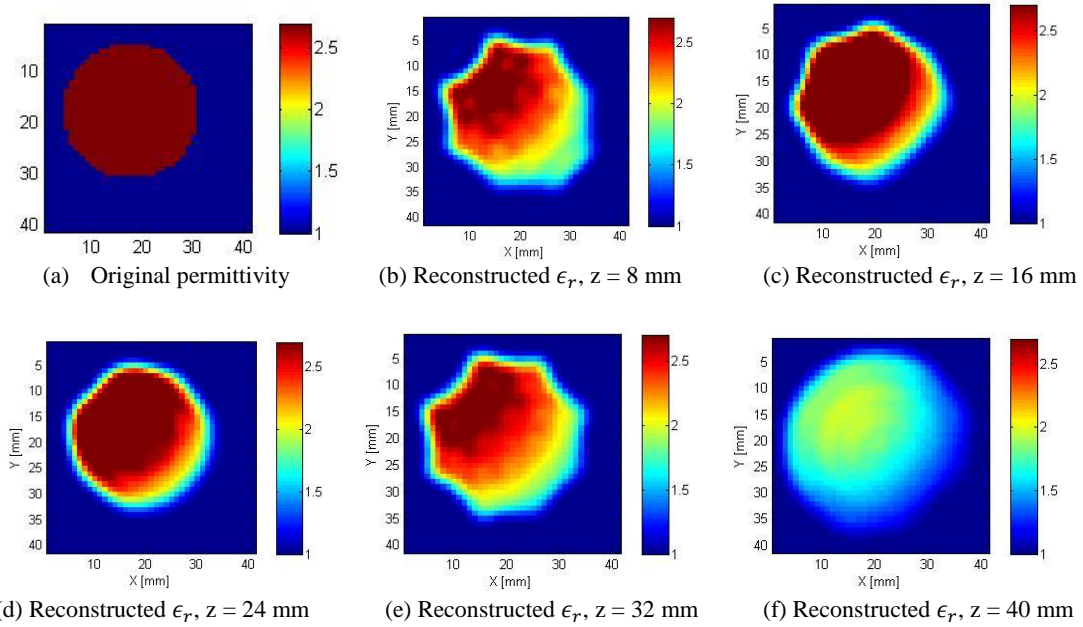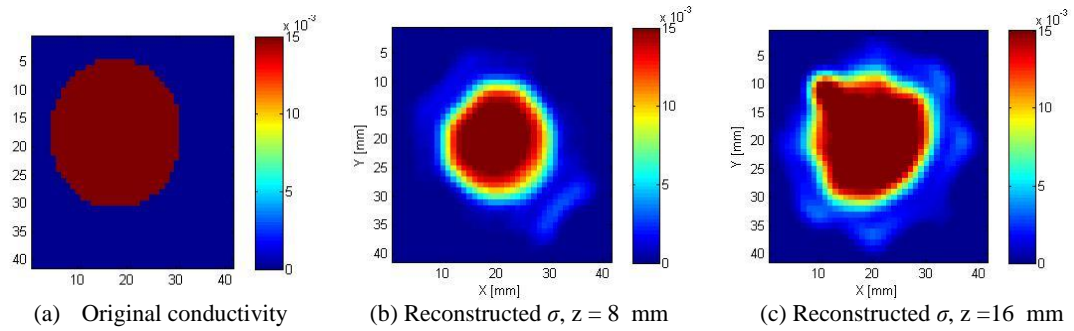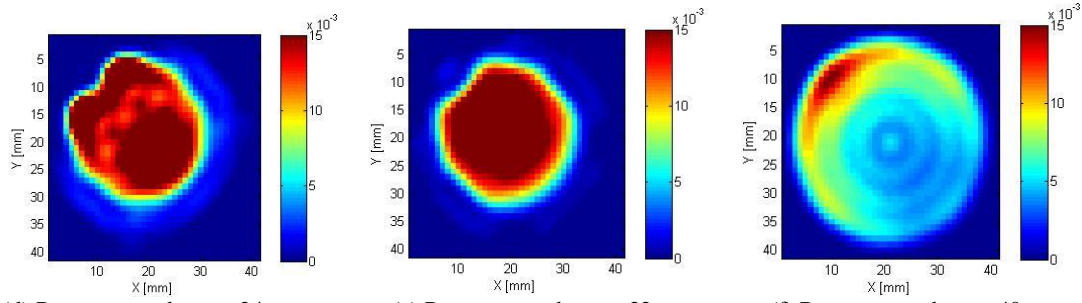
Figure 6.2-6 2D representation of reconstructed images of the single target object using accurate antenna modelling. (a) is the original model of conductivity. (b)-(g) Reconstructed conductivity images of simulated data with 10 iteration are shown in different heights using centre frequency and FWHM 1.0 GHz

As seen in Figure 6.2-5 and Figure 6.2-6, the permittivity and conductivity of the object have been reconstructed accurately.

By reviewing the results in chapter 6.2.1, it can be concluded that the large number of attempts are required for the reconstruction process in order to obtain converged results. Therefore, the process has been extended to ten iterations instead of five. The reconstructed dielectric properties are demonstrating reasonable alignment with original model as shown in Figure 6.2-4.

6.2.2 Simulation and measurement of a cup of sunflower oil with air as background

In this section, microwave measurements have been made to enable comparison with simulation data. Before the measurement process, the system should be calibrated. Therefore, the frequency values have been set to frequencies between 500 MHz and 6 GHz, 801 measuring points and IF bandwidth 1 KHz (this selection has been done to have better accuracy, however this choice increases measurement time). Afterwards the calibration settings have been saved with a traceable name and measurement process starts by running the algorithm with saved parameters. During the measurement process, four sets of measurements have been performed for collecting the reference and object data. Then, the collected S-parameters have been plotted with MATLAB and analysed. The most accurate data, which are compatible with the correct measured S-parameters has been selected for reconstruction.

The 3D FDTD simulation of the target object is the same as the simulation which is described in Table 6.2-1. The target object has been located at 10 mm offset in the y direction from the centre of reconstruction domain.

In first attempt, the pulse centre frequency has been set to 1.5 GHz with a FWHM 1.0 GHz. Table 6.2-2 represents the FDTD modelling and reconstruction settings for measurement data at centre frequency 1.5 GHz and FWHM 1.0 GHz. The result of the reconstructed dielectric properties didn't converge well.

Table 6.2-2 FDTD modelling and reconstruction parameters for measurement data of a cup of oil by the setup using centre frequency 1.5GHz and FWHM 1.0 GHz as reconstruction frequency components

|	
FDTD spatial grid	160×160×160
Grid cell size (in x, y and z direction)	1 mm
Number of CPML	11
Simulation time	8.0×10^{-9} sec
Source function	Gaussian envelope sinusoidal function
Source centre frequency	3.0 GHz
Source FWHM bandwidth	3.0 GHz
Antenna model	Thin wire monopole
Feed model	50 Ω RVS
Background (air)	ϵ_r=1.0, $\sigma = 0.0$ S/m

In order to rectify this issue, the same parameters described in Table 6.2-2 has been used for FDTD modelling and reconstruction settings, but the centre frequency 900 MHz and narrower bandwidth 300MHz have been selected as frequency components in the reconstruction algorithm. The conductivity and permittivity have been reconstructed, however considerable artifacts in antenna positions have been observed. The results of simulated and measured data have been shown in Figure 6.2-7 - Figure 6.2-13.
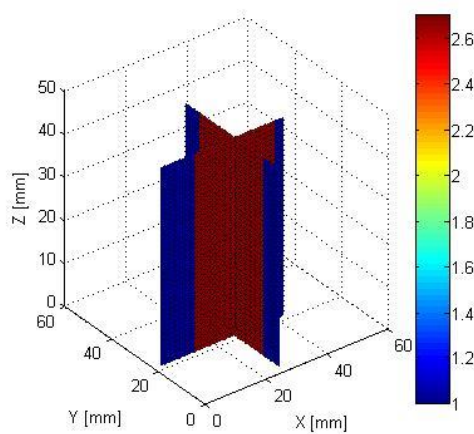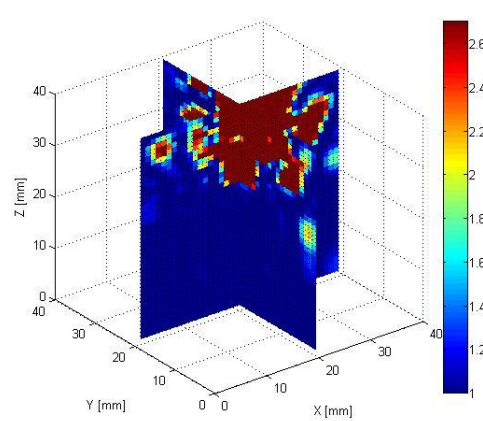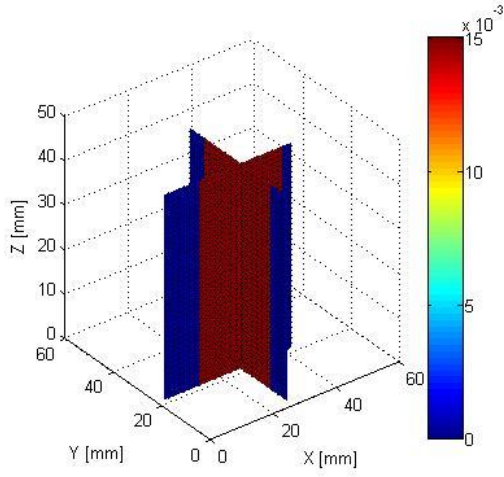

(a)   Original ϵ_r model
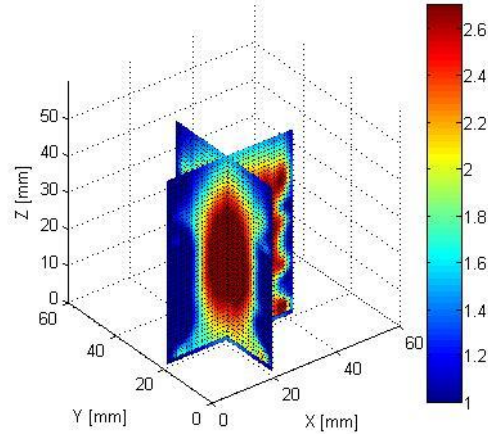
(b) Reconstructed ϵ_r for simulated data at 1.0 GHz
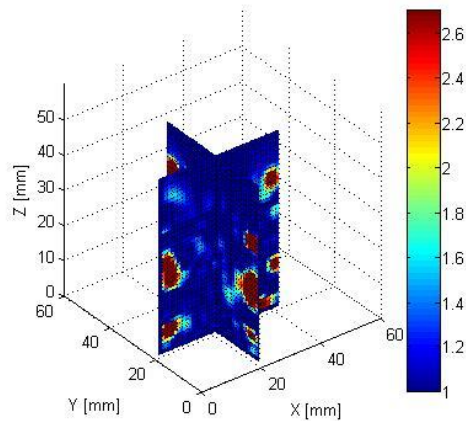
(c) Reconstructed ϵ_r for measured data at 1.5 GHz

(d) Reconstructed ϵ_r for measured data at 900 MHz

(a)   Original σ model
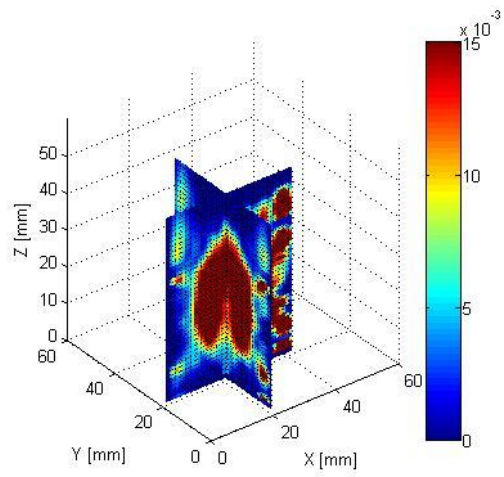
(b) Reconstructed σ for simulated data at 1.0 GHz
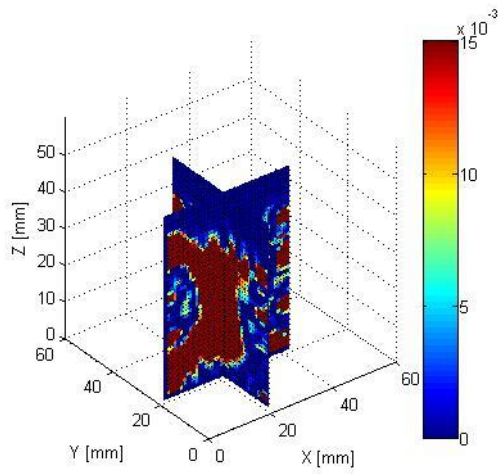
(c) Reconstructed σ for measured data at 1.5 GHz
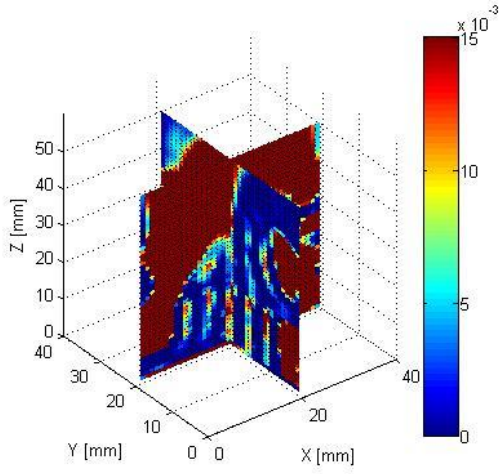
(d) Reconstructed σ for measured data at 900 MHz

Figure 6.2-7 3D representation of the original model and simulated and measured reconstruction
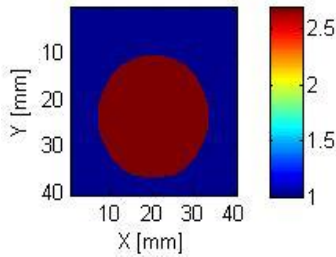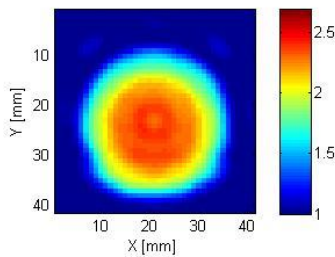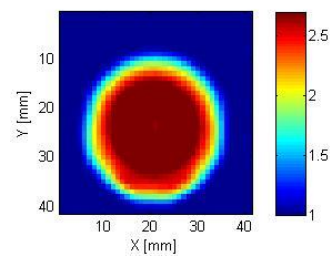
(a)   Original permittivity

(b) Reconstructed ϵ_r, z =8 mm

(c) Reconstructed ϵ_r, z =16 mm
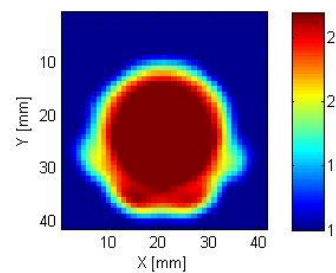
(d) Reconstructed ϵ_r, z =24 mm
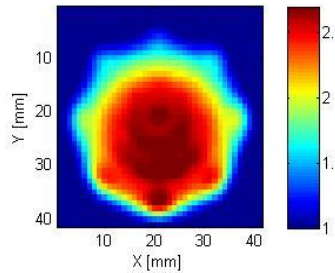
(e) Reconstructed ϵ_r, z =32 mm
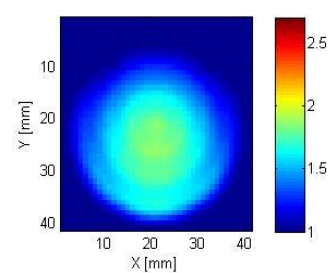
(f) Reconstructed ϵ_r, z =40 mm

Figure 6.2-8 2D representation of reconstructed images of the single target object using accurate antenna modelling.
(a) is the original model of permittivity. (b)-(g) Reconstructed permittivity images of simulated data with 10 iteration
are shown in different heights using centre frequency and FWHM 1.0 GHz.

(a) Original permittivity   (b) Reconstructed ϵ_r, z =8 mm   (c) Reconstructed ϵ_r, z =16 mm

(d) Reconstructed ϵ_r, z = 24 mm   (e) Reconstructed ϵ_r, z = 32 mm   (f) Reconstructed ϵ_r, z = 40 mm
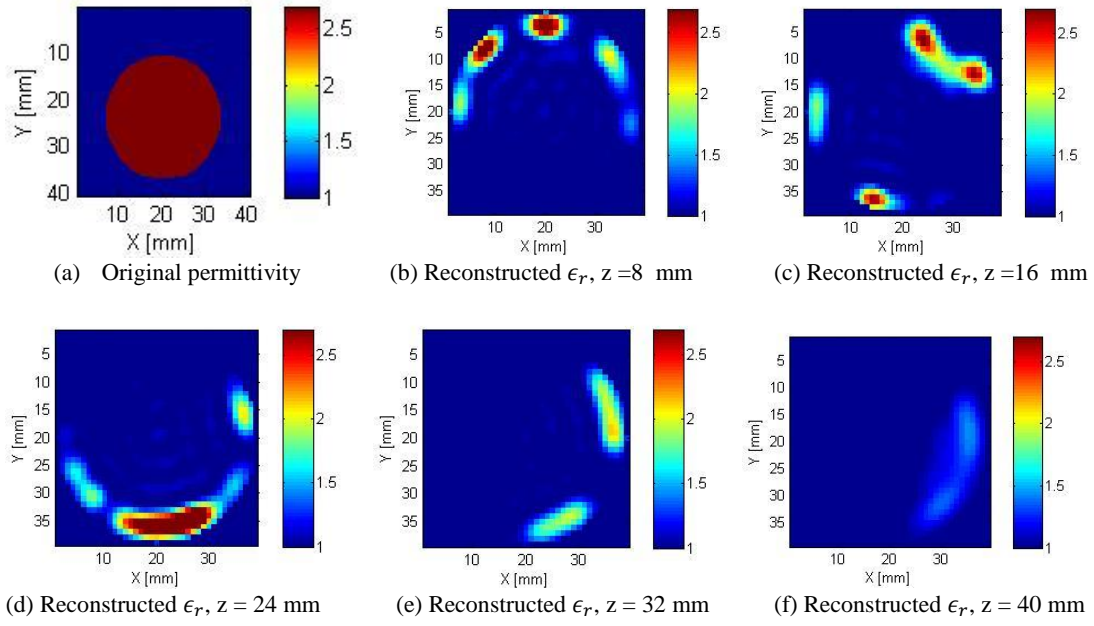
Figure 6.2-9 2D representation of reconstructed images of the single target object using accurate antenna modelling. (a) is the original model of permittivity. (b)-(g) Reconstructed permittivity images of measured data with 6 iteration are shown in different heights using centre frequency 1.5 GHz, FWHM 1.0 GHz

(a) Original permittivity   (b) Reconstructed ϵ_r, z = 8 mm   (c) Reconstructed ϵ_r, z =16 mm

(d) Reconstructed ϵ_r, z = 24 mm   (e) Reconstructed ϵ_r, z = 32 mm   (f) Reconstructed ϵ_r, z = 40 mm

Figure 6.2-10 2D representation of reconstructed images of the single target object using accurate antenna modelling. (a) is the original model of permittivity. (b)-(g) Reconstructed permittivity images of measured data with 6 iteration are shown in different heights using centre frequency 900 MHz, FWHM 300 MHz

As seen above, there are significant artifacts in reconstructed dielectric properties even in narrower bandwidth. As seen, just the boundaries have been reconstructed. This can be due to antenna modelling and also switching problem during the measurements. Also, the size of the imaged object and frequency values can impose errors in the reconstructed images.

(a)   Original conductivity (b) Reconstructed σ, z = 8 mm (c) Reconstructed σ, z =16 mm

(d) Reconstructed σ, z = 24 mm (e) Reconstructed σ, z = 32 mm (f) Reconstructed σ, z = 40 mm

Figure 6.2-11 2D representation of reconstructed images of the single target object using accurate antenna modelling. (a) is the original model of conductivity. (b)-(g) Reconstructed conductivity images of simulated data with 10 iteration are shown in different heights using centre frequency and FWHM 1.0 GHz

(a)   Original conductivity (b) Reconstructed σ, z = 8 mm (c) Reconstructed σ, z =16 mm

(d) Reconstructed σ, z =24 mm (e) Reconstructed σ, z =32 mm (f) Reconstructed σ, z =40 mm

Figure 6.2-12 2D representation of reconstructed images of the single target object using accurate antenna modelling. (a) is the original model of conductivity. (b)-(g) Reconstructed conductivity images of measured data with 6 iteration are shown in different heights using centre frequency 1.5 GHz, FWHM 1.0 GHz

| (a) Original conductivity | (b) Reconstructed σ, z =8 mm | (c) Reconstructed σ, z = 16 mm |

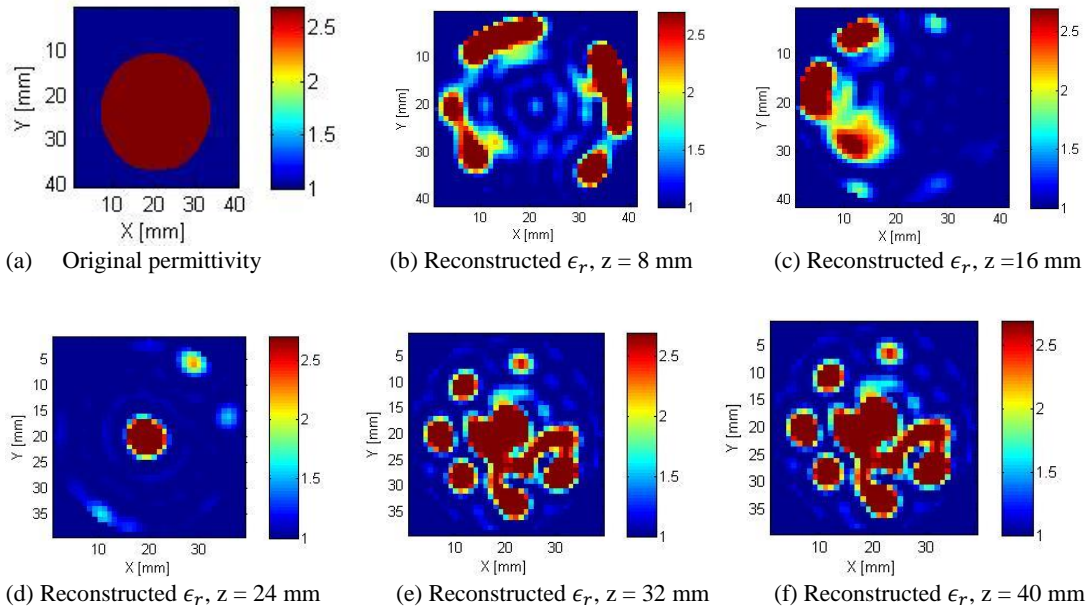(d) Reconstructed σ, z =24 mm   (e) Reconstructed σ, z = 32 mm   (f) Reconstructed σ, z = 40 mm
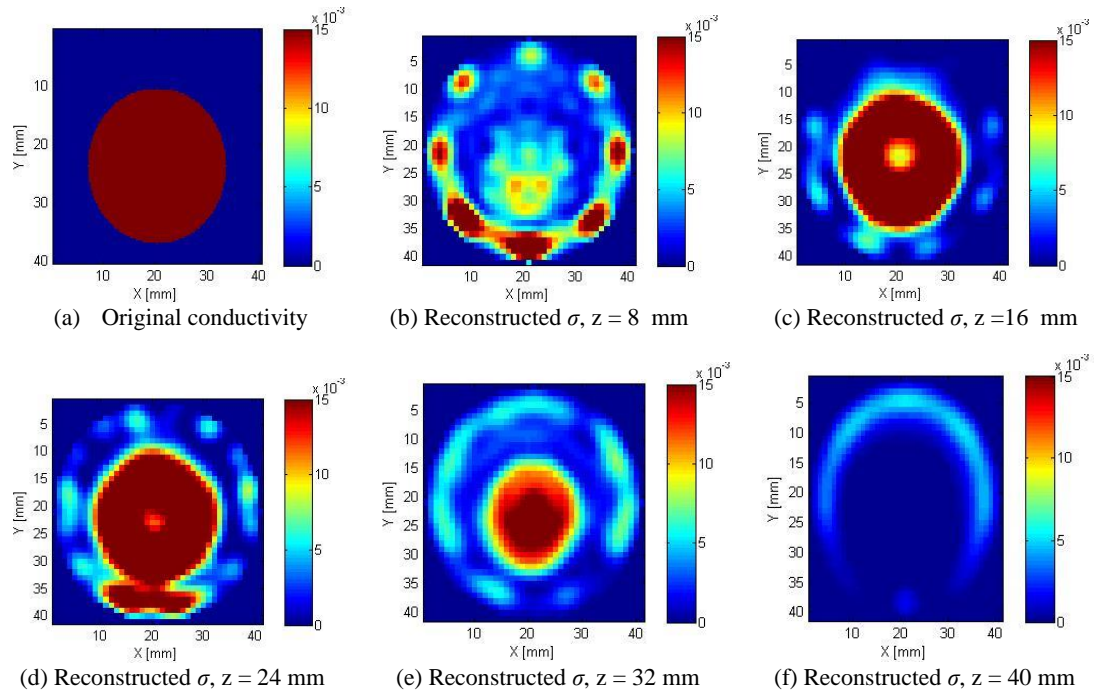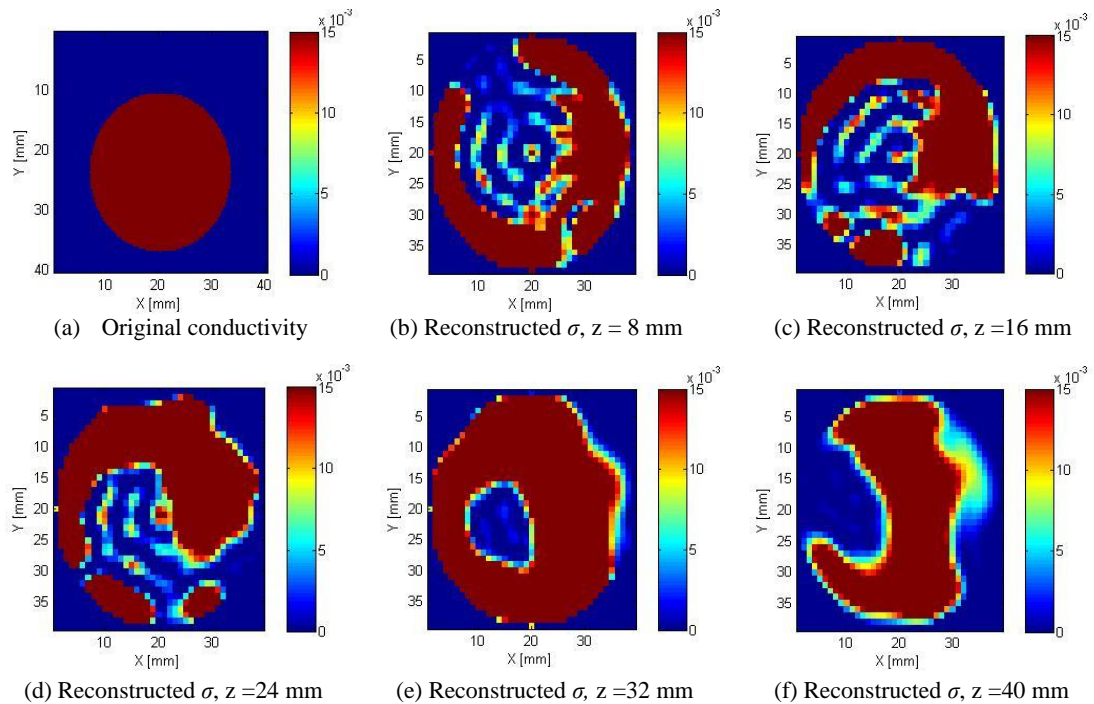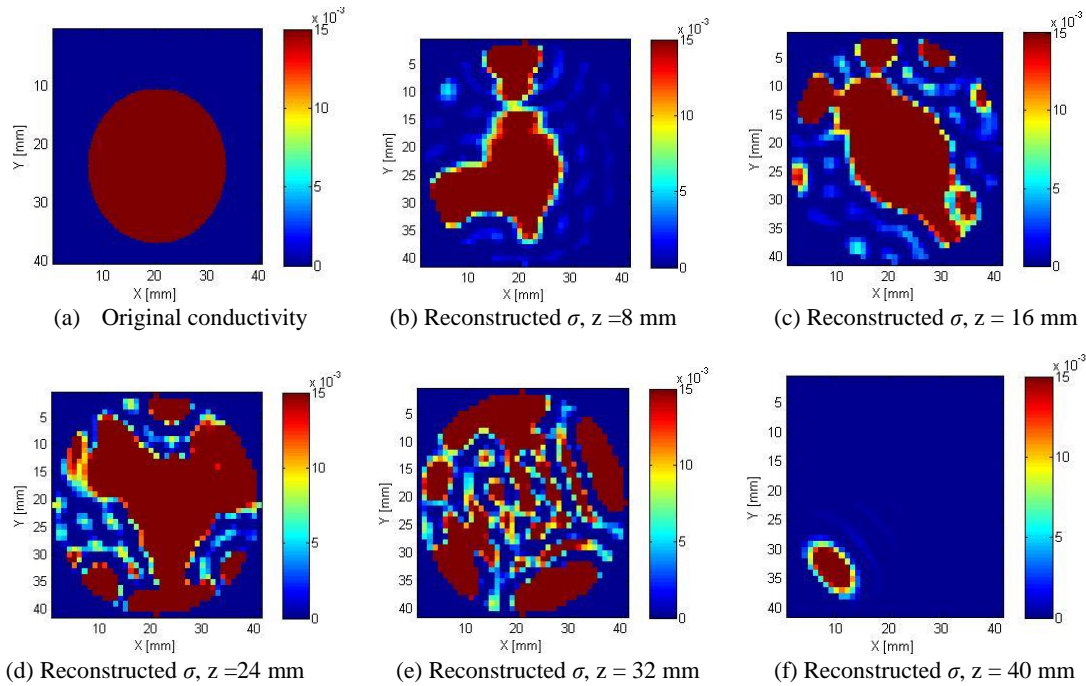
Figure 6.2-13 2D representation of reconstructed images of the single target object using accurate antenna modelling. (a) is the original model of conductivity. (b)-(g) Reconstructed conductivity images of measured data with 6 iteration are shown in different heights using centre frequency 900 MHz, FWHM 300 MHz

It has been observed that in comparison with reconstructed permittivity, the reconstructed conductivity does have better outcomes by using centre frequency 900Hz and FWHM 300 MHz, however it has less spatial accuracy. The target object is resolved in the centre of reconstruction domain, however there are still lots of artefacts. The reason can be due to the placing of the object close to the antenna arrays in the reconstruction domain. Consequently, the reflected artifacts from the target object increase and then significant noise appears in reconstruction results.

In the following of the part 6.2.1, the microwave measurements have been performed with modelled phantoms in section 6.2.2. By plotting and analysing the measured S-parameters in MATLAB it has been observed that some of them are not compatible with the rest measurement data set. This situation is probably due to switching malfunction. It can happen when one or two antennas try to switch and there seems to be a problem with switching matrix system and as a consequence of this problem the antennas cannot switch perfectly. According to this issue, the collected data has been evaluated by MATLAB and more accurate data have been selected for reconstructing. Besides, the simulation of the imaged object is made by the algorithm to compare with the measurement results.

The reconstruction process is completed and several frequencies and bandwidth have been tried in order to find the more accurate reconstruction settings. The illustrated results in Figure 6.2-7 indicates that measurement results don't show good similarity to the reconstruction of the simulation results.

By reviewing the obtained reconstruction results, it is inferred that the modelled measurement system in the reconstruction algorithm introduce several errors in the reconstruction results. The antenna position, feed source and imprecise parameters also can impose errors and inaccuracies in the results. Regarding to this matter, the frequency components, position of the monopole antennas and length of them in the algorithm should be set in the same order as existent measurement setup to avoid misplacement errors.

It should be taken into account that any movement in the hardware system imposes errors in the measurement process as well, so the setup system needs to be fixed and stable to keep away the movement errors.

As seen in Figure 6.2-15, the simulated S12 corresponding to the measured data indicates that the amplitude levels and resonances in the simulated data are approximately similar to the measured data. Also, the measuring process starts from 500 MHz and there are some removed data in S-parameters in the simulation and measurement data. Furthermore, the simulated S12 implies some numerical errors in the mentioned frequency span and the data below -80 dB considered not reliable. One of the parameter that can effect on this, is simulation time. In addition other parameters can be weakness of the signal at the end of Gaussian pulses and there is basically no DC components in the pulse. Consequently, there is no DC signal and the numerical error exists in the simulated S-parameters.
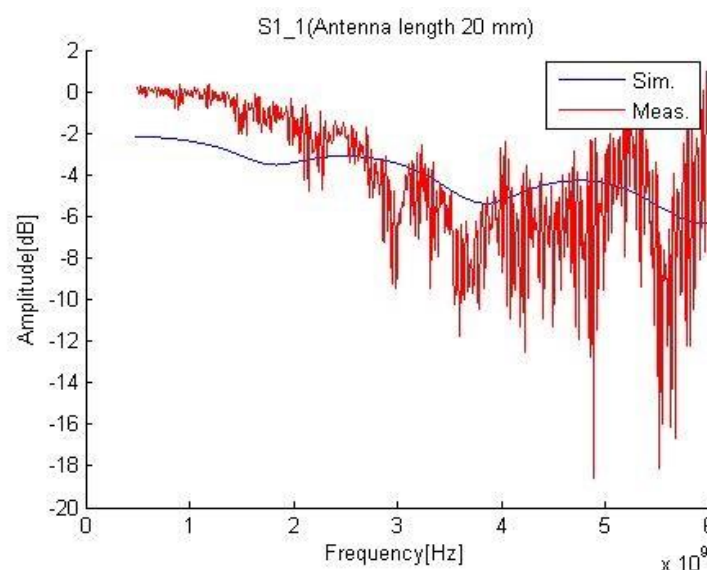

Figure 6.2-14 S1_1 parameters for Measured and Simulated data by algorithm (actual length)
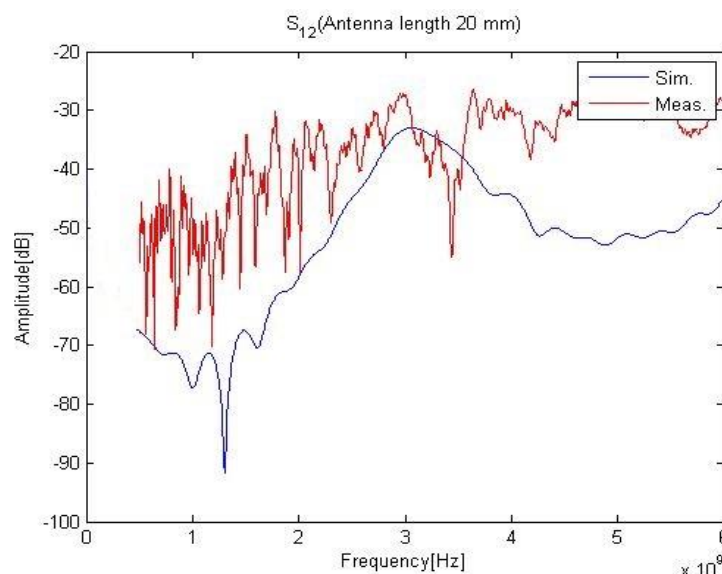
Figure 6.2-15 S1_2 parameters for Measured and Simulated data by algorithm (actual length)

6.2.3 Simulation of a cup of sunflower oil with water as background

In this section, the simulation has been performed to reconstruct a single object immersed in the water. **Error! Reference source not found.** shows the FDTD odelling and reconstruction settings.

Table 6.2-3 3D FDTD modelling and reconstruction parameter setting for single object immersed in water as background

FDTD spatial grid	160×160×160
Grid cell size (in x, y and z direction)	1 mm
Number of CPML	11
Simulation time	20×10^{-9} sec
Source function	Gaussian envelope sinusoidal function
Source centre frequency	3.0 GHz
Source FWHM bandwidth	3.0 GHz
Antenna model	Thin wire monopole
Feed model	50 Ω RVS
Background (water)	ϵ_r=77.0, $\sigma = 0.05$ S/m

Since the water has high permittivity, the FDTD simulation of water requires much more time and shorter time stepping in comparison to air in the FDTD algorithm. Therefore, the simulation time is set to 20×10^{-9} seconds and centre frequency and FWHM of 150 MHz have been selected as reconstruction frequencies. The imaging results are shown in Figure 6.2-17 and Figure 6.2-18.

(a) Original ϵ_r model   (b) Reconstructed ϵ_r for simulated data at 150 MHz
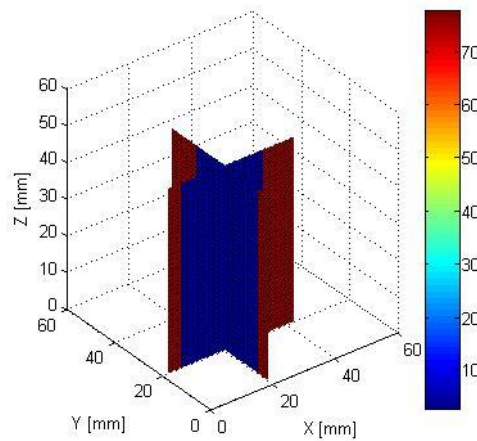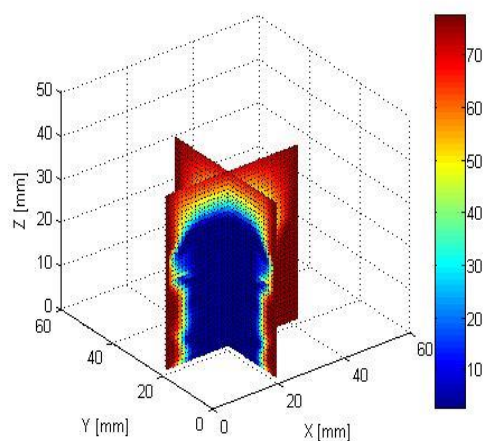
(a) Original σ model   (b) Reconstructed σ for simulated data at 150 MHz
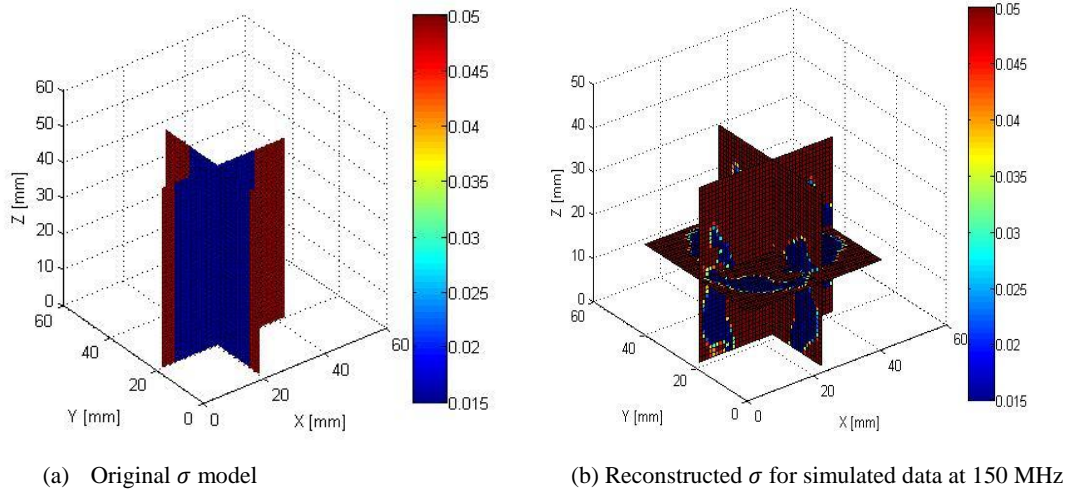
Figure 6.2-16 3D representation of the original model and simulated reconstruction

(a) Original permittivity   (b) Reconstructed ϵ_r, z =6 mm   (c) Reconstructed ϵ_r, z = 12 mm

(d) Reconstructed ϵ_r, z = 18 mm   (e) Reconstructed ϵ_r, z = 24 mm   (f) Reconstructed ϵ_r, z = 30 mm

Figure 6.2-17 2D representation of reconstructed images of the single target object immersed in water as matching liquid using accurate antenna modelling. (a) is the original model of permittivity. (b)-(g) Reconstructed permittivity images of simulated data with 7 iteration are shown in different heights using centre frequency and FWHM 150 MHz

(a) Original conductivity (b) Reconstructed σ, z = 6 mm (c) Reconstructed σ, z = 12 mm

(d) Reconstructed σ, z = 18 mm (e) Reconstructed σ, z = 24 mm (f) Reconstructed σ, z = 30mm

Figure 6.2-18 2D representation of reconstructed images of the single target object immersed in water as matching liquid using accurate antenna modelling. (a) is the original model of conductivity. (b)-(g) Reconstructed conductivity images of simulated data with 7 iteration are shown in different heights using centre frequency and FWHM 150 MHz

The reconstruction of the target object immersed in water as matching liquid is shown above. Figure 6.2-16 shows the overview of the object sliced in the objects centre. As shown in Figure 6.2-17, the reconstructed simulated data for permittivity shows good similarity with original model and the object has been reconstructed well in right size and position. Howeve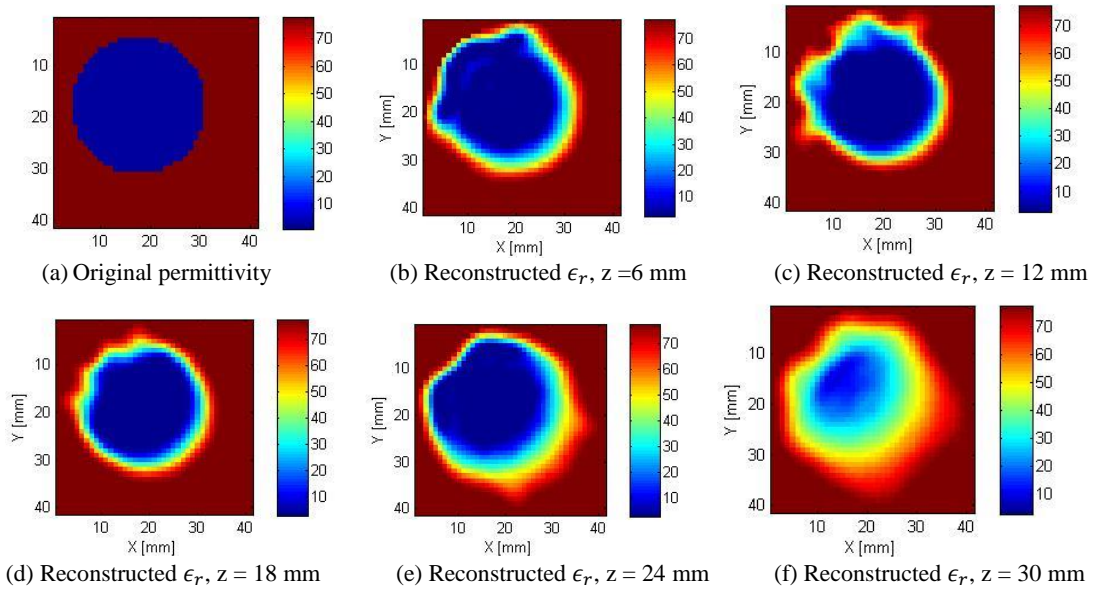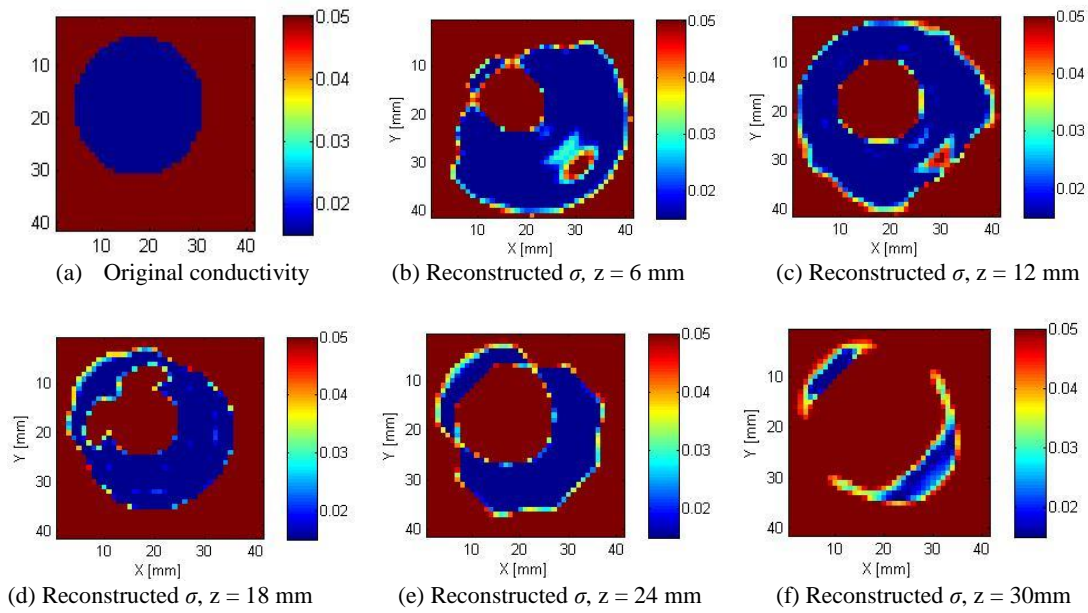r, the reconstructed conductivity suffers from ringing artefact illustrated in Figure 6.2-18. A pulse frequency and bandwidth 150 MHz have been utilized as reconstruction frequencies. The object becomes hollow even by using the lower frequency components.

The less accuracy and ringing artifacts of the reconstructed dielectric properties can be due to the difference in the real and imaginary part of the complex permittivity between the object and background medium. Consequently, the errors in the reconstruction of the real part effects the reconstruction of the imaginary part. Therefore, only boundaries have been detected and the single object became hollow. The low contrast in reconstructed conductivity is due to some restriction in the reconstruction algorithm. Besides, it is obtained that the frequency values should be set to less than 1 GHz to resolve the bigger objects when there is a high permittivity matching liquid in the background medium.

6.3 Reconstruction of two objects immersed in vegetable oil

According to different simulations it is obtained that there is a need for matching liquid to minimize the reflections from skin and increase the resolution of image. So, the dielectric properties of matching liquid should be selected properly. The lossiness of the selected matching liquid should be as low as possible to have a significant contrast between healthy and malignant tissue. By considering this fact, vegetable oil is used as matching liquid in the background in this section. Two objects with dielectric properties of ϵ_r=2.0 and $\sigma = 0.03$ S/m are simulated in the simulation space. **Error! Reference ource not found.** represents the FDTD simulation and reconstruction settings.

Table 6.3-1 3D FDTD modelling and reconstruction parameter setting for two objects immersed in vegetable oil as background

FDTD spatial grid	160×160×160
Grid cell size (in x, y and z direction)	1 mm
Number of CPML	11
Simulation time	4.0×10^{-9} sec
Source function	Gaussian envelope sinusoidal function
Source centre frequency	3.0 GHz
Source FWHM bandwidth	3.0 GHz
Antenna model	Thin wire monopole
Feed model	50 Ω RVS
Background (vegetable oil)	ϵ_r=2.7, $\sigma = 0.015$ S/m

As shown in Figure 6.3-1 the simulated data illustrated acceptable agreement between original and reconstructed objects. In addition, by analysing the reflection and transmission coefficients in MATLAB it is found that S11 parameter has a very low amplitude in comparison to S12. As a consequence by disabling the S11 parameter in the reconstruction algorithm the reflection artefacts reduce and the noise values eliminate in the reconstructed images.

(a)   Original ϵ_r model   (b) Reconstructed ϵ_r for simulated data at 1.0 GHz
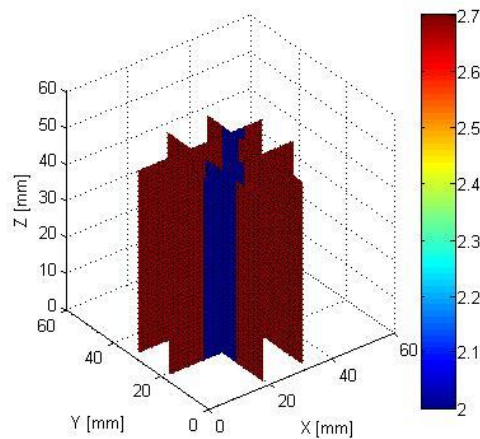
(a) Original σ model
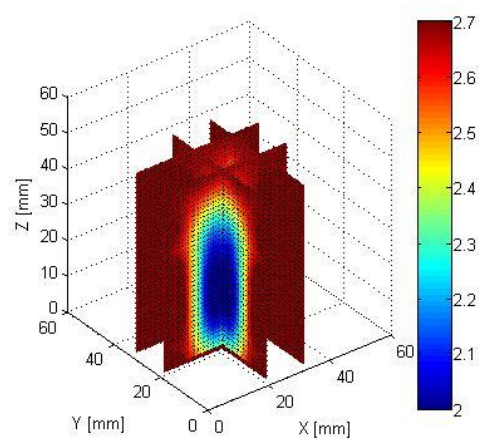
(b) Reconstructed σ for simulated data at 1.0 GHz
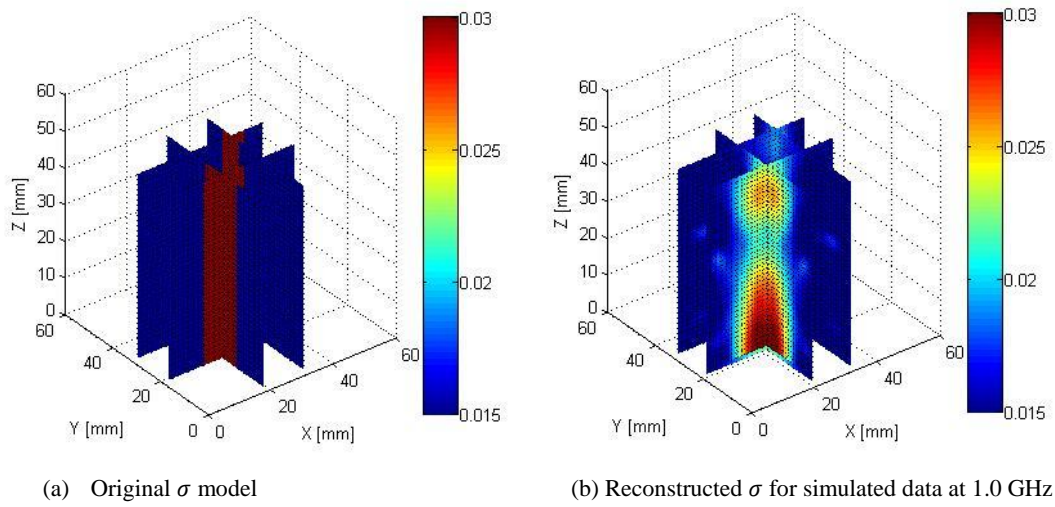
Figure 6.3-1 3D representation of the original model and simulated reconstruction

(a) Original permittivity

(b) Reconstructed ϵ_r, z = 8 mm

(c) Reconstructed ϵ_r, z =16 mm

(d) Reconstructed ϵ_r, z = 24 mm

(e) Reconstructed ϵ_r, z = 32 mm

(f) Reconstructed ϵ_r, z =40 mm

Figure 6.3-2 2D representation of reconstructed images of the two target objects immersed in vegetable oil as matching liquid using accurate antenna modelling. (a) is the original model of permittivity. (b)-(g) Reconstructed permittivity images of simulated data with 10 iteration are shown in different heights using centre frequency and FWHM 1.0 GHz.

(a) Original conductivity

(b) Reconstructed σ, z =8 mm

(c) Reconstructed σ, z = 16 mm

(d) Reconstructed σ, z =24 mm   (e) Reconstructed σ, z = 32 mm   (f) Reconstructed σ, z = 40 mm

Figure 6.3-3 2D representation of reconstructed images of the two target objects immersed in vegetable oil as matching liquid using accurate antenna modelling. (a) is the original model of conductivity. (b)-(g) Reconstructed conductivity images of simulated data with 10 iteration are shown in different heights using centre frequency and FWHM 1.0 GHz

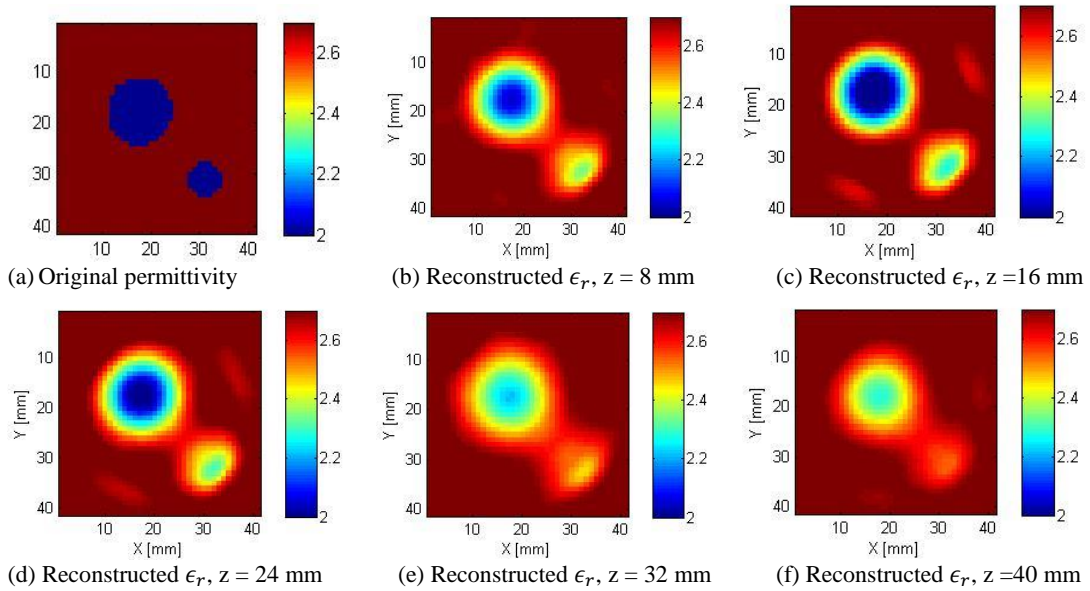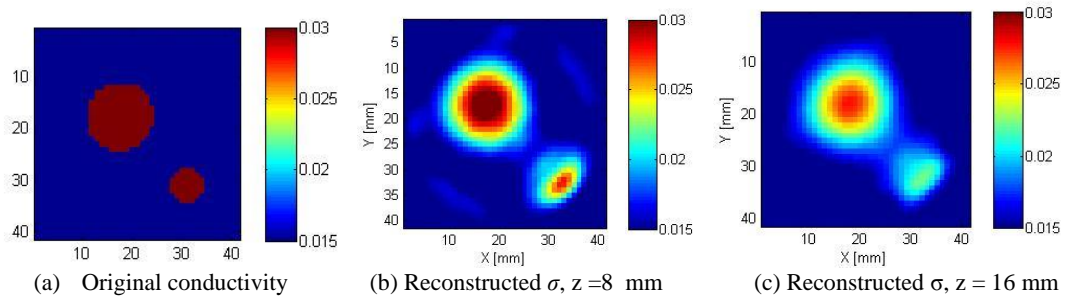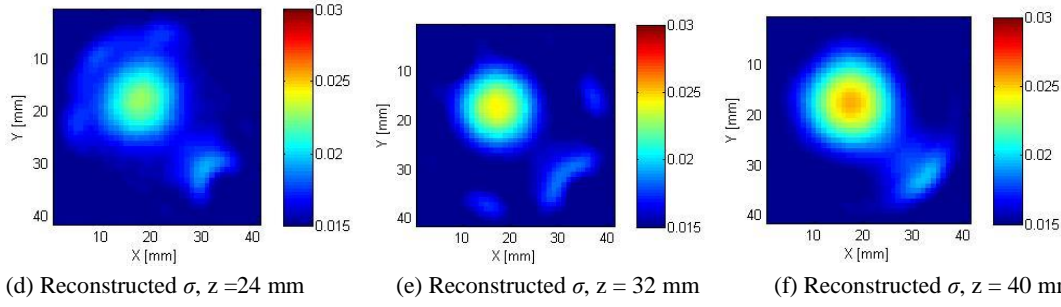In this case, the reconstruction algorithm is using centre frequency 1.0 GHz with FWHM 1.0 GHz. Ten iterations have been made on a 3 mm grid cell size. The reconstruction for simulated data has been performed successfully in 9 hours and the objects have been resolved well in correct positions and sizes. However, conductivity values for smaller object has less accuracy in comparison to permittivity values. Several attempts have been performed to find the appropriate background medium in section 6.3. Finally, by choosing the oil as matching liquid two objects with approximately known dielectric properties and distinct sizes in two different positions have been detected.

As it can be observed in Figure 6.3-2 and Figure 6.3-3, there are no ringing or reflection artefacts, and two objects are resolved well in the right position.

In all of the simulation in part 6.2 and 6.3 the spatial resolution of the grid cell size is set to 3 mm and reasonable images are concluded in the simulated reconstructions, thus all the images have been reshaped and rescaled accordingly to make the comparison easy and understandable.

In addition, a good idea to obtain the accurate reconstruction parameters is to start the reconstruction process with small number of iterations. Since the reconstruction process requires a long time, this choice gives the possibility to find the appropriate reconstruction settings in shorter time. After finding the suitable parameters the number of iterations can be increased to derive desired images.

6.4 Reconstruction of complex models including inclusions

In this section, complex simulations have been made to model a bigger object including one inclusion. In the following, the simulation of a healthy breast including two tumours has been performed to investigate the performance of the reconstruction algorithm. The reconstruction settings and results are discussed more in details.

6.4.1 Simulation of a large object including one inclusion

A more complex simulation has been performed to verify the performance of the reconstruction algorithm. For this purpose, the simulation is performed defining a large object including one inclusion. The large object has dielectric properties $\epsilon_r = 2$ and $\sigma = 0.03$ S/m. The radius of the large object is set to 50 mm and has heights of 100 mm. The small object introducing tumour has the radius of 10 mm, heights of 60 mm and dielectric values $\epsilon_r = 12$ and $\sigma = 0.09$ S/m. The target object was assumed to be immersed in vegetable oil as matching liquid and dielectric values of $\epsilon_r = 2.7$ and σ = 0.015 S/m. Table 6.4-1 describes the FDTD modelling and reconstruction setting.

Table 6.4-1 3D FDTD modelling and reconstruction parameter setting for one large object including one inclusion immersed in vegetable oil as background

FDTD spatial grid	160×160×160
Grid cell size (in x, y and z direction)	1 mm
Number of CPML	11
Simulation time	8.0×10^{-9} sec
Source function	Gaussian envelope sinusoidal function
Source centre frequency	3.0 GHz
Source FWHM bandwidth	3.0 GHz
Antenna model	Thin wire monopole
Feed model	50 Ω RVS
Background (vegetable oil)	ϵ_r=2.7, $\sigma = 0.015$ S/m

(a)   Original ϵ_r model

(b) Reconstructed ϵ_r for simulated data at 1.5 GHz

(a)   Original σ model
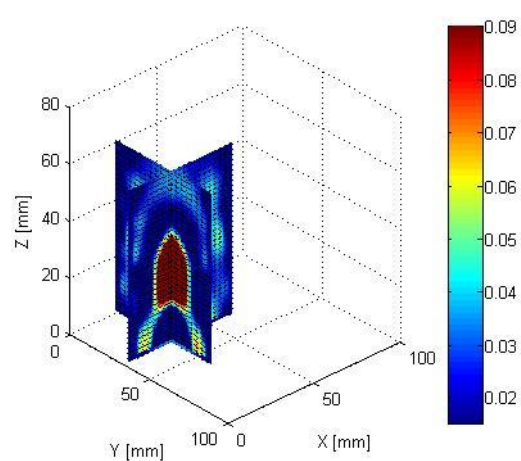
(b) Reconstructed σ for simulated data at 1.5 GHz

Figure 6.4-1 3D representation of the original model and simulated reconstruction

(a) Original permittivity   (b) Reconstructed ϵ_r, z = 8 mm   (c) Reconstructed ϵ_r, z =16 mm

(d) Reconstructed ϵ_r, z = 24 mm   (e) Reconstructed ϵ_r, z = 32 mm   (f) Reconstructed ϵ_r, z =40 mm

Figure 6.4-2 2D representation of reconstructed images of the simulated breast model within one tumour immersed matching liquid using accurate antenna modelling. (a) is the original model of permittivity. (b)-(g) Reconstructed permittivity images of simulated data with 20 iteration are shown in different heights using centre frequency 1.5 GHz and FWHM 1.0 GHz

(a)   Original conductivity   (b) Reconstructed σ, z = 8 mm   (c) Reconstructed σ, z = 16 mm

(d) Reconstructed σ, z = 24 mm   (e) Reconstructed σ, z = 32 mm   (f) Reconstructed σ, z = 40 mm
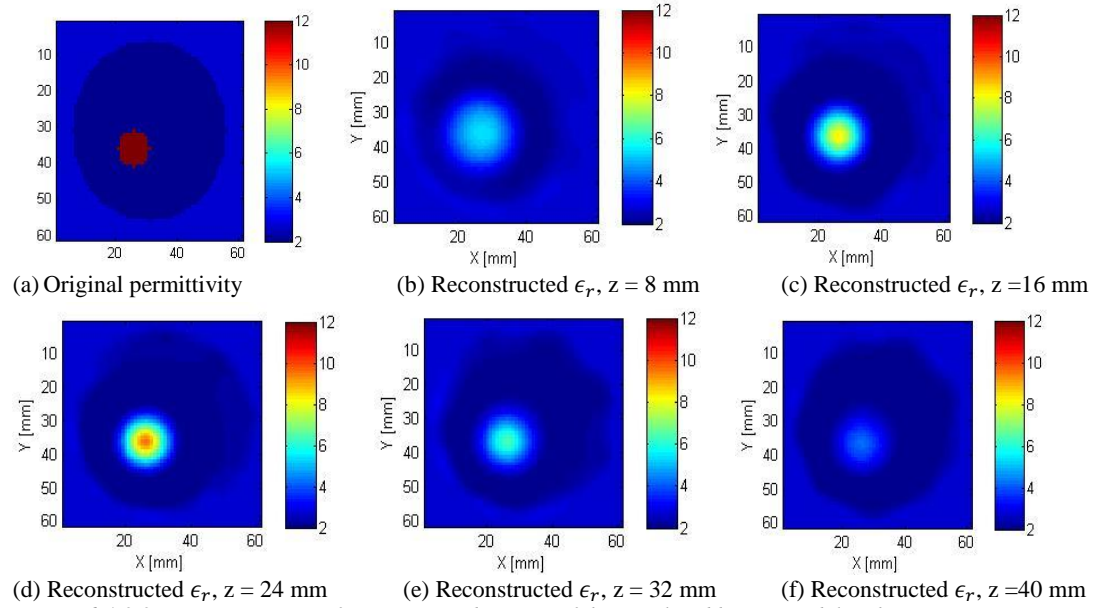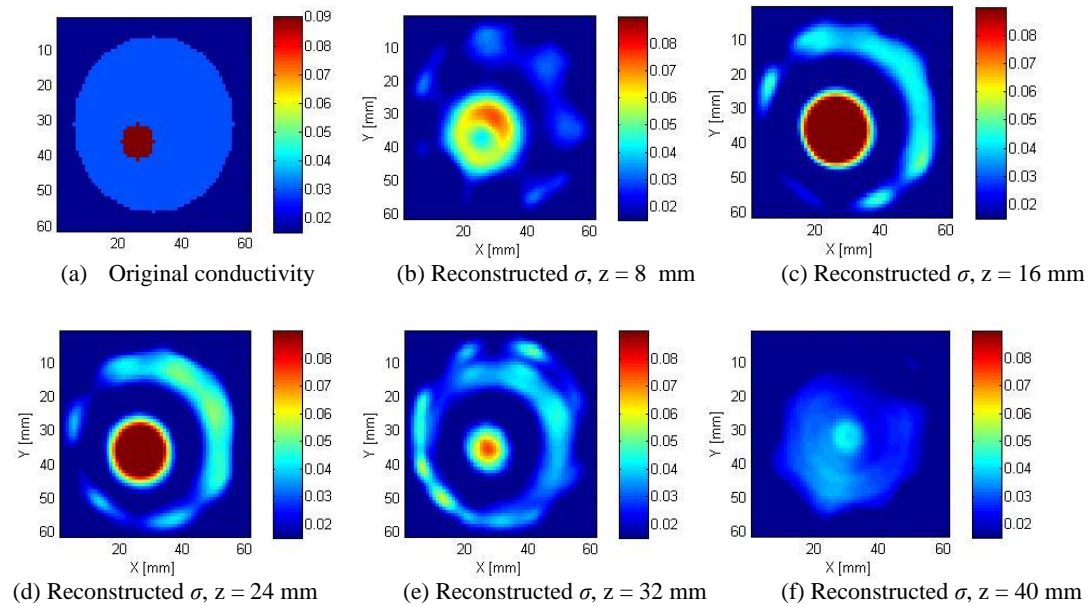
Figure 6.4-3 2D representation of reconstructed images of the simulated breast model within one tumour immersed matching liquid using accurate antenna modelling. (a) is the original model of permittivity. (b)-(g)Reconstructed conductivity images of simulated data with 20 iteration are shown in different heights using centre frequency 1.5 GHz and FWHM 1.0 GHz

In the beginning of the reconstruction process it has been assumed that the object has not been located in the simulation space (simulated calculation) but after locating the object (measurement calculation), the difference between the simulated and measurement data is very large. When the reconstruction process started to reconstruct the object and iterates, the difference between the simulation and measurement data became minimum and it was continued to reach the minimum value. In this case, the simulation shows that it is suitable to use a centre frequency 1.5 GHz with a FWHM 1.0 GHz. Twenty iterations have been made on 2 mm grid cell size in the algorithm. It took about 15 hours to complete the reconstruction process. The permittivity and conductivity values are reconstructed in the correct position of the object as shown in
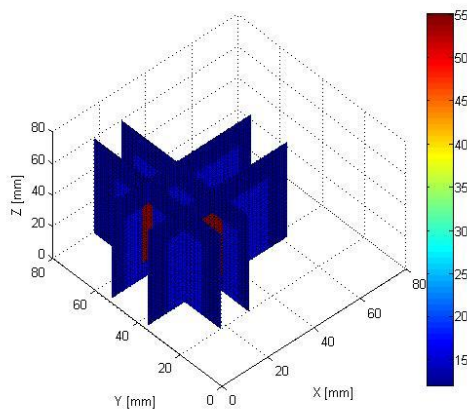
figure 6.4-2 and 6.4-3. However there is still some artefacts in reconstructed conductivity of large object.

6.4.2 Simulation of a real breast model within two tumours

In this part of work, simulation of a realistic breast phantom with two inclusions have been made. To this end, the simulation has been performed with a large object introducing healthy breast including two tumours. The large object has dielectric properties $\epsilon_r = 15$, $\sigma = 0.4$ S/m, heights of 90 mm and the radius of 50 mm. The small objects introducing tumours had the radius of 10 mm and 5 mm, heights of 60 mm and dielectric properties $\epsilon_r = 55$ and $\sigma = 1.0$ S/m. The target object is assumed to be immersed in matching liquid which has dielectric values of $\epsilon_r = 12$ and $\sigma = 0.3$ S/m. The FDTD modelling and reconstruction setting are summarized in Table 6.4-2.

Table 6.4-2 3D FDTD modelling and reconstruction parameter setting for realistic breast phantom including two tumours

FDTD spatial grid	160×160×160
Grid cell size (in x, y and z direction)	1 mm
Number of CPML	11
Simulation time	8.0×10^{-9} sec
Source function	Gaussian envelope sinusoidal function
Source centre frequency	3.0 GHz
Source FWHM bandwidth	3.0 GHz
Antenna model	Thin wire monopole
Feed model	50 Ω RVS
Background	$\epsilon_r = 12$, $\sigma = 0.3$ S/m

(a)   Original ϵ_r model
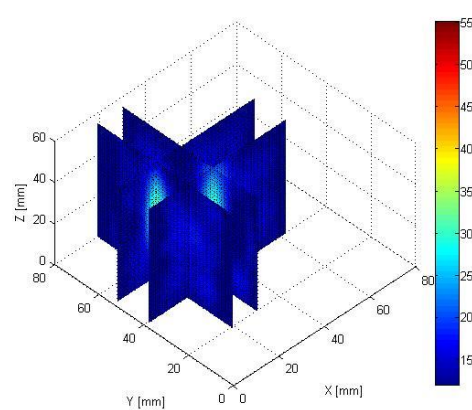
(b) Reconstructed ϵ_r for simulated data at 900 MHz
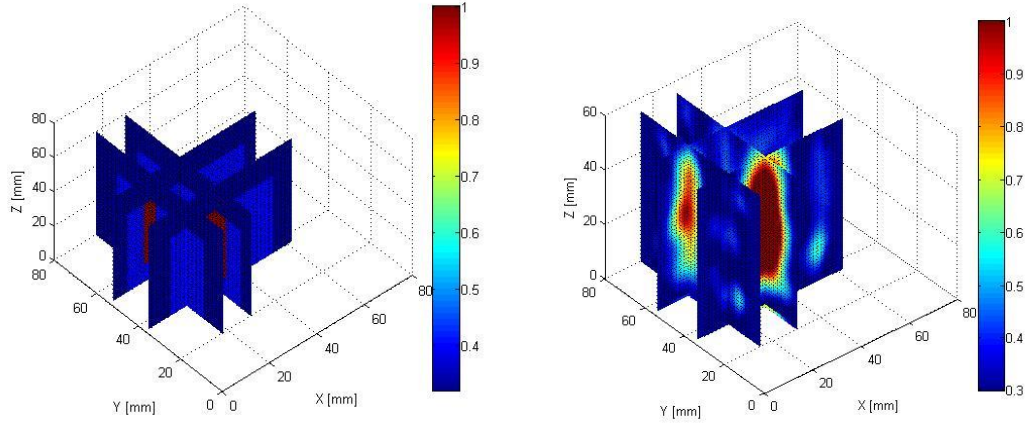
(a)   Original σ model

(b) Reconstructed σ for simulated data at 900 MHz

Figure 6.4-4 3D representation of the original model and simulated reconstruction

(a) Original permittivity

(b) Reconstructedϵ_r, z = 9 mm

(c) Reconstructedϵ_r, z = 18 mm

(d) Reconstructedϵ_r, z = 27 mm

(e) Reconstructedϵ_r, z = 36 mm

(f) Reconstructedϵ_r, z = 45 mm

Figure 6.4-5 2D representation of reconstructed images of the simulated breast model within one tumour immersed in matching liquid using accurate antenna modelling. (a) is the original model of permittivity. (b)-(g) Reconstructed permittivity images of simulated data with 20 iteration are shown in different heights using centre frequency and FWHM 900 MHz

(a)   Original conductivity

(b) Reconstructed σ, z = 9 mm

(c) Reconstructed σ, z = 18 mm

(d) Reconstructed σ, z = 27 mm   (e) Reconstructed σ, z = 36 mm   (f) Reconstructed σ, z = 45 mm
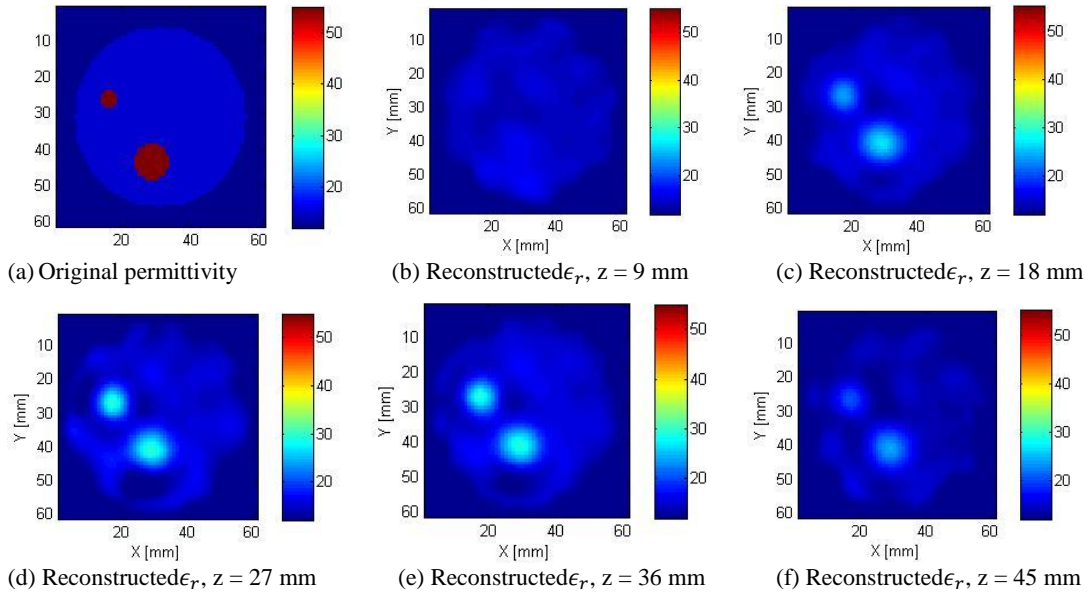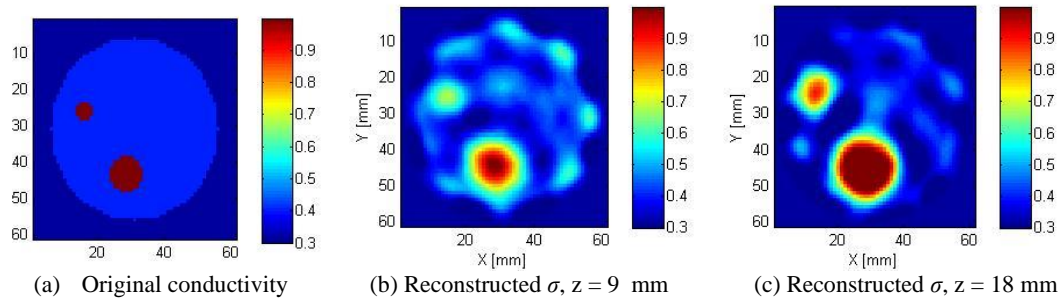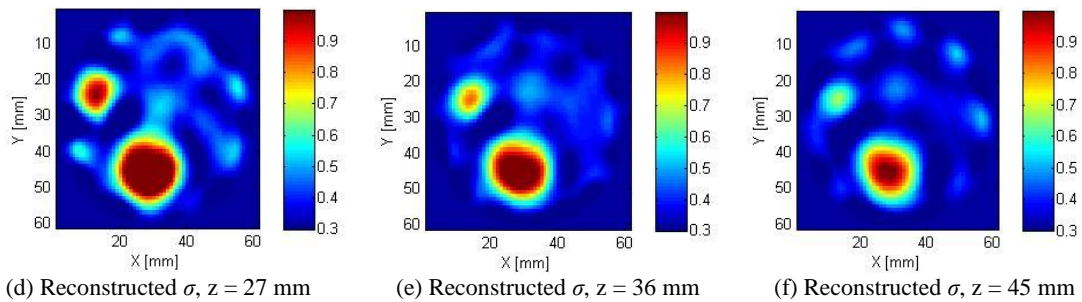
Figure 6.4-6 2D representation of reconstructed images of the simulated healthy breast model including two tumours immersed in matching liquid using accurate antenna modelling. (a) is the original model of conductivity. (b)-(g)Reconstructed conductivity images of simulated data with 20 iteration are shown in different heights using centre frequency and FWHM 900 MHz

Figure 6.4-5 and Figure 6.4-6 showing that the dielectric profiles of the objects have acceptable reconstruction results. It is found that for resolving the large objects the centre frequency should be set to low frequency contents in order to increase reconstruction accuracy. Because in this case the penetrated wavelength is high enough to detect the bigger object. Also, the lower frequencies include less amount of noise components and in result the artefacts have been reduced in this case. However, in the case of smaller objects, higher centre frequency and larger bandwidth have been expected. So, here the centre frequency and FWHM has been set to 900 MHz. The reconstruction process has been performed by 20 iterations on 2 mm grid cell size. The procedure took 20 hours to be completed. The results show good agreement between original model and reconstructed images.

The algorithm is potential to reconstruct the simulated and measurement data. To this end, selection of the values for dielectric properties and frequency components should be appropriate in order to get accurate reconstruction settings. In other words, selecting accurate data would remove one of the error sources. The reconstruction algorithm is very sensitive to the adjusted parameters, antenna modelling and measurement errors, i.e., the precise choice of the dielectric properties for matching liquid and target objects and modelled breast phantoms is leading to get the most successful and desired outcomes.

Here, the values for target objects and matching liquids have not been measured by dielectric probes and the values have been selected from literature studies.

It can be concluded that for improving the accuracy of the reconstruction results, more coupling liquids should be found for the simple breast phantoms. By evaluating the outcomes, appropriate matching liquid can be obtained for complex phantoms. In addition, for successful reconstructions different frequency values have to be tested for several modelled phantoms to give tuned parameters for the reconstruction of phantoms in different sizes and background medium.

Here, the performance of the algorithm is examined for several composition of female's breast tissues with different sizes that include one or two tumours.

To this end two different simulations have been made to model a large object including one inclusion and a female's breast tissue within two tumours.

The plotted images in Figure 6.4-1 gives a good overview of the original model and reconstructed objects of a bige object including one inclusion. To acquire acceptable results different number of simulations with different positions of tumours have been fulfilled in the section 6.4.2. Finally, the tumours have been detected in the defined positions successfully.

In the reconstruction process of section 6.4, the spatial resolution of the grid cell size is set to 2 mm. Although this selection of grid cell size increases the reconstruction time, the results show very good match with original models.

6.5 Evaluation of the simulated and measurement data

The results of the several reconstructions have been compared by plotting the functional values in MATLAB. As described previously, a cost functional has been defined to minimize the difference between measured and simulated electric fields on the receiver antennas. The reconstruction process has been followed while the minimum possible difference between the measured and simulated data has been acquired. Afterwards, according to the minimum difference the reconstruction profile has been updated and the procedure has been repeated while achieving the acceptable accuracy. The main and important point here is the dropped functional values in Figure 6.5-1, where it describes that the functional values of different simulated and measured data minimized and the reconstruction process has converged. However, the reconstruction of measured data for a cup of oil failed in 6th iteration. The same situation has also been happened for the simulation data for a cup of oil immersed in water which failed in 7th iteration.
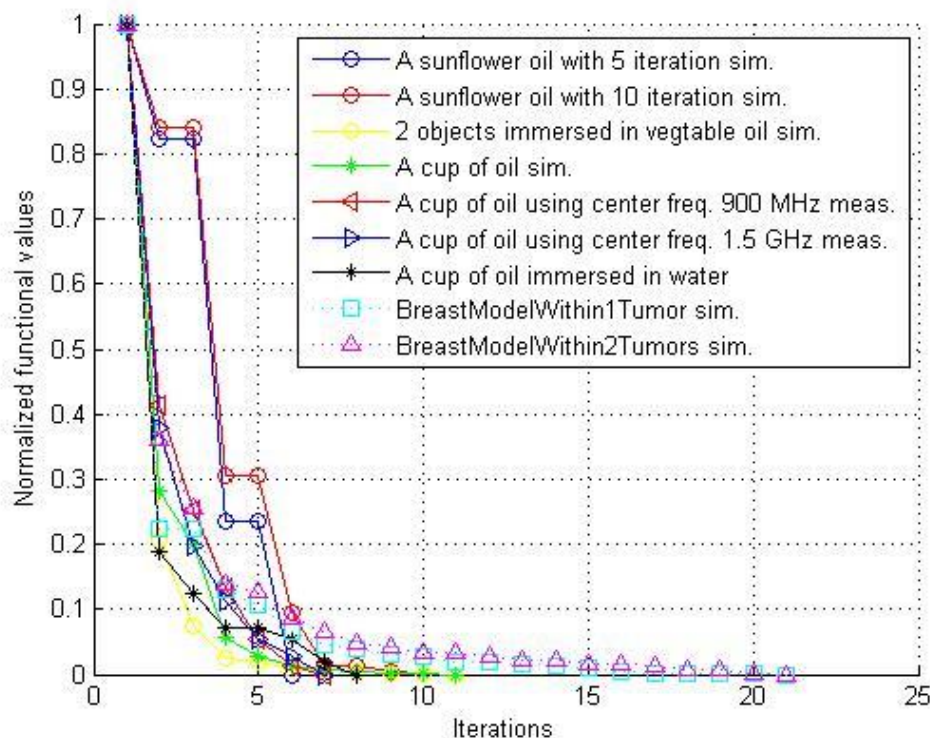

Figure 6.5-1 Normalized functional values for 3D reconstruction as a function of iteration number for the simulated and measured data.

7 Conclusion and Future work

In this master work several simulations including different dielectric properties and frequency components have been performed to model different objects in medium. It has been observed that using the accurate antenna length maximizes the accuracy of reconstructed images. The S11 parameter has been disabled in order to reduce the noise components in the reconstructed images.

The grid cell size and antenna modelling have been modelled accurately according to the available setup system. Different simulations for reconstruction have been performed by current algorithm and successful results have been obtained.

In the following, microwave measurements have been made to enable comparison with simulation data. The object is not resolved well in the supposed position in the measurement results. This implies that the reconstruction algorithm is very sensitive to antenna modelling, measurement errors and frequency settings. Therefore, finding the tuned parameters for reconstruction algorithm is leading to have successful reconstructed dielectric properties.

Successful reconstructions results have been acquired by using the FDTD model and vegetable oil as background medium for two objects with different sizes and dielectric properties of ϵ_r=2.0, $\sigma = 0.3$ S/m.

For a big object which has been made of sunflower oil and immersed in water as matching liquid, it is obtained that the reconstruction frequency components should be below 1.0 GHz to reach accurate imaging results. However there were significant artifacts in the reconstructed conductivity results.

Furthermore, it has been found that different size of objects with different dielectric properties need particular frequency components to be resolved.

The numerically breast model including tumours has been imaged and promising results have been obtained for permittivity and conductivity values. In addition, it has been experienced that, increasing the number of iterations improves the accuracy of reconstruction results significantly.

In future works advanced breast phantom should be manufactured in order to compare the performance of the system and reconstruction algorithm with numerically modelled breast tissues.

There were also some problems with the reconstructed conductivity which were not accurate in some cases, this can be due to the large difference in real and imaginary part of the complex permittivity. Changing the reconstruction frequency and reducing physical boundaries for reconstruction domain can be solutions to improve the accuracy of reconstructed conductivity. Also, making sure that the permittivity and conductivity solutions have been connected is another other possibility to obtain more accurate reconstructed conductivity results.

The switching matrix system should be replaced with a developed one to avoid measurement errors.

Besides, the modelling errors, noise and inaccuracy in antenna positioning can be the reason of some faults in reconstruction process.

Overall, it has been observed that the system is robust enough and by selecting the appropriate reconstruction parameters in the reconstruction algorithm accuracy of the reconstructed conductivity values can be improved. The algorithm and system, both have a great potential to be utilized as a complementary method to mammography modality in order to provide desired sensitivity and specificity to detect malignant tissues in breast during early stages.

References

[1] Hinrikus, H., Riipulk J., Wiley Encyclopedia of Biomedical Engineering, Microwave Imaging, John Wiley & Sons, Inc .April 2006

[2] K.L. Carr, P. Cevasco, P. Dunlea, and J. Shaeffer. Radiometric sensing: an adjuvant to mammography to determine breast biopsy. In Microwave Symposium Digest. 2000 IEEE MTT-S International, volume 2, pages 929–932 vol.2, June 2000.

[3] Meaney, P., M. Fanning, D. Li, S. Poplack, and K. Paulsen, "A clinical prototype for active microwave imaging of the breast," IEEE Transactions on Microwave Theory and Techniques, Vol. 48, No. 11, 1841-1853, 2000.

[4] S. Noghanian, A. Sabouni, S. Pistorius, A Numerical Approach to Microwave Imaging based on Genetic Algorithm optimization, in: Proc. of SPIE Symposium Health Montitoring and Diagnostics, San Diego, CA, 2006.

[5] E.C. Fear, P.M. Meaney, M.A. Stuchly, Microwaves for breast cancer detection, IEEE Potentials 22 (1) (2003) 12–18.

[6] L.E. Larsen and J.H. Jacobi, "Microwave scattering parameter imagery of an isolated canine kidney," Medical Physics, vol. 6, pp. 394–403, 1979.

[7] S.Y. Semenov, R.H. Svenson, A.E. Boulyshev, A.E. Souvorov, V.Y. Borisov, Y. Sizov, A.N. Starostin, K.R. Dezern, G.P. Tatsis, and V.Y. Baranov. Microwave tomography: two-dimensional system for biological imaging. Biomedical Engineering, IEEE Transactions on, 43(9):869–877, Sept 1996.

[8] Fhager A., Padhi S. K.,Howard J., ''3D image Reconstruction in Microwave Tomography Using an Efficient FDTD Model'', IEEE Antenna and Wireless Propagation Letters, Vol.8,2009

[9] P.M. Meaney, K.D. Paulsen, A. Hartov, and R.K. Crane. An active microwave imaging system for reconstruction of 2-d electrical property distributions. Biomedical Engineering, IEEE Transactions on, 42(10):1017–1026, Oct. 1995.

[10] P.M. Meaney, M.W. Fanning, Dun Li, S.P. Poplack, and K.D. Paulsen. A clinical prototype for active microwave imaging of the breast. Microwave Theory and Techniques, IEEE Transactions on, 48(11):1841–1853, Nov. 2000.

[11] P.M. Meaney, K.D. Paulsen, and J.T. Chang. Near-field microwave imaging of biologically-based materials using a monopole transceiver system. Microwave Theory and Techniques, IEEE Transactions on, 46(1):31–45, Jan 1998.

[12] P.M. Meaney, K.D. Paulsen, J.T. Chang, M.W. Fanning, and Alexander Hartov. Nonactive antenna compensation for fixed array microwave imaging. ii. Imaging results. Medical Imaging, IEEE Transactions on, 18(6):508–518, June 1999.

[13] S. Y. Semenov, A. E. Bulyshev, A. E. Souvorov, A. G. Nazarov, Y. E. Sizov, R. H. Svenson, V. G. Posukh, A. V. Pavlovsky, P. N. Repin and G. P. Tatsis, "Three-dimensional microwave tomography: Experimental imaging of phantoms and biological objects," IEEE Trans. Microwave Theory Tech., vol. 48, pp. 1071–1074, 2000.

[14] A. E. Bulyshev, A. E. Souvorov, S. Y. Semenov, V. G. Posukh and Y. E. Sizov, "Three-dimensional vector microwave tomography: theory and computational experiments," Inv. Probl., vol. 20, pp. 1239– 1259, Aug, 2004.

[15] Z. Q. Zhang and Q. H. Liu, "Three-dimensional nonlinear image reconstruction for microwave biomedical imaging," IEEE Trans. Biomed. Eng., vol. 51, pp. 544–548, Mar. 2004.

[16] A. Abubakar and P. M. van den Berg, "Iterative forward and inverse algorithms based on domain integral equations for three-dimensional electric and magnetic objects," J. Com. Phys., vol. 195, pp. 236–262, Mar. 2004.

[17] Fhager A., ''Microwave Tomography,'' Ph.D. Thesis, Chalmers University of Technology, Sweden, 2006.

[18] American cancer society, available at http://www.cancer.org/cancer

[19] Swedish Cancer Registry: Statistics on Public Health and Social Care 2011, http://www.socialstyrelsen.se/

[20] Mostovoy A. , 'Thermograpphy Clinic Inc.', available at http://www.drmostovoy.com/

[21] J. G. Elmore, M. B. Barton, V. M. Moceri, S. Polk, P. J. Arena, and S. W. Fletcher, "Ten-year risk of false positive screening mammograms and clinical breast examinations," N. Engl. J. Med., vol. 338, no. 16, pp. 1089–1096, 1998.

[22] P. T. Huynh, A. M. Jarolimek, and S. Daye, "The false-negative mammogram," Radiographic, vol. 18, no. 5, pp. 1137–1154, 1998.

[23] R. J. Jackman, K. W. Nowels, J. Rodriguez-Soto, F. A. Marzoni Jr., S. I. Finkelstein, and M. J. Shepard, "Stereotactic, automated, large-core needle biopsy of no palpable breast lesions: False-negative and histologic underestimation rates after long-term follow-up," Radiology, vol. 210, pp. 799–805, 1999.

[24] Handbook of Biological Effects of Electromagnetic Fields, 2nd ed., C. Polk and E. Postow, Eds., CRC, New York, 1996.

[25] M. Lazebnik1, L. McCartney, D. Popovic, C.B. Watkins, M.J. Lindstrom, J. Harter, S. Sewall, A. Magliocco, J.H. Booske1, M. Okoniewski, and S.C. Hagness, "A large-scale study of the ultrawideband microwave dielectric properties of normal breast tissue obtained from reduction surgeries," Phys. Med.Biol., vol. 52, pp. 2637-2656, 2007.

[26] Noghanian S, Microwave Tomography for Biomedical Quantitative Imaging. J Elec Electron 1:e107. doi:10.4172/2167-101X.1000e107, July,2012.

[27] Breast anatomy, http://www.geronguide.com/gallery/index.php/Breast-Cancer/breast-anatomy-02

[28] S. Gabriel, R. W. Lau, and C. Gabriel" The dielectric properties of biological tissues: III. Parametric models for the dielectric spectrum of tissues Phys. Med. Biol. 41 2271–93, 1996b.

[29] Mahfouz M.,Kuhn M., To G., '' The Future of Ultra Wideband Systems in Medicine: Orthopedic Surgical Navigation,'' University of Tennessee, USA,Aug.2011.

[30] P. Debye, Polar molecules, Dover Publications, London, 1929.

[31] K. S. Cole and R. H. Cole, "Dispersion and absorption in dielectrics I. Alternating current characteristics," J. Chem. Phys., vol. 9, pp. 341, 1941.

[32] K. S. Cole and R. H. Cole, "Dispersion and absorption in dielectrics II.Direct current characteristics," J. Chem. Phys., vol. 10, pp. 98, 1942.

[33] D. K. Cheng, Field and wave electromagnetics. Addison-Wesley Publishing Company, Inc., second ed., 1989.

[34] K. S. Yee, "Numerical solution of initial boundary value problems involving Maxwell's equations in isotropic media," Antennas and Propagation, IEEE Transactions on, vol. 14, pp. 302–307, May. 1966.

[35] Rylander T.,Bondeson A., Ingelstrom P." Computational Electromagnetics'' second edition,2007.

[36] A. Taflove and M. E. Brodwin, "Numerical solution of steady-state electromagnetic scattering problems using the time-dependent Maxwell's equations," Microwave Theory and Techniques, IEEE Transactions on, vol. 23, pp. 623–630, Aug. 1975.

[37] M. Mansourabadi and A. Pourkazemi," FDTD hard source and soft source reviews and modifications," Progress In Electromagnetics Research C, Vol. 3, 143–160, 2008.

[38] J Köster, "Image reconstruction and FDTD modelling of antenna array for 3D microwave tomography," Master thesis, Chalmers University of Technology, Sweden, March .2011.

[39] A. Taflove and S. C. Hagness, Computational Electrodynamics: The Finite-Difference Time-Domain Method. Artech House Inc, third ed., 2005.

[40] G. Mur, "Absorbing boundary conditions for the finite difference approximation of the time domain electromagnetic field equations", IEEE Trans. Electromagn. Compat., vol. EMC-23, pp.377 -382 1981

[41] J.-P. Berenger, "A perfectly matched layer for the absorption of electromagnetic waves," Journal of Computational Physics, vol. 114, no. 2, pp. 185–200, 1994.

[42] D. S. Katz, E. T. Thiele, and A. Taflove, "Validation and extension to three dimensions of the Berenger PML absorbing boundary condition for FD-TD meshes," IEEE Microwave and Guided Wave Letters, vol. 4, no. 8, pp. 268–270, 1994.

[43] J. A. Roden and S. D. Gedney, "Convolution PML (CPML): An efficient FDTD implementation of the CFS-PML for arbitrary media," Microwave and Optical Technology Letters, vol. 27, no. 5, pp. 334–339, 2000.

[44] J. C. Logan J. W. Rockway,''Dipole and Monopole Antenna Gain and Effective Area for Communication Formulas,''Technical report 1756, 1997.

[45] W.C. Chew, "Waves and Fields in Inhomogeneous Media'', Wiley-IEEE Press, 1999.

[46] J. Hadamard, "Lectures on Cauchy's Problem in Linear Partial Differential Equations", Yale University Press, New Haven, 1923.

[47] Chew WC, Wang YM, Reconstruction of two-dimensional permittivity distribution using the distorted Born iterative method. IEEE Trans Med Imaging 9: 218-225, 1990.

[48] Otto G, Chew WC," Microwave inverse scattering - local shape function imaging for improved resolution of strong scatters". IEEE Trans Microwave Theory Tech 42: 137-141, 1994.

[49] E. Polak, Computational methods in optimization: A unified approach, New York: Academic, 1971.

[50] M. Miyakawa, "Tomographic measurement of temperature change in phantoms of the human body by chirp radar-type microwave computed tomography," Med. Biol. Eng. Comput., vol. 31, pp. S31–S36, 1993.

[51] A.C. Kak, M. Slaney, Principles of Computerized Tomographic Imaging, Society of Industrial and Applied Mathematics, 2001.

[52] M. Slaney, A. C. Kak and L. E. Larsen, "Limitations of Imaging with First-Order Diffraction Tomography," IEEE Trans. Microwave Theory Tech., vol. 32, pp. 860-873, Aug. 1984.

[53] J. C. Bolomey, C. Pichot, G. Garboriaud , "Planar microwave imaging camera for biomedical applications: Critical and prospective analysis of reconstruction algorithms, 'Radio. Sc., vol. 26, n0.2, pp 541–549, 1991.